Astronomy & Astrophysics manuscript no. SMM1_C2H3NO_isomers
March 3, 2022
©ESO 2022

arXiv:2012.15672v1 [astro-ph.SR] 31 Dec 2020

The prebiotic molecular inventory of Serpens SMM1

I. An investigation of the isomers CH_3NCO and $HOCH_2CN$

N.F.W. Ligterink[1], A. Ahmadi[2], A. Coutens[3], Ł. Tychoniec[2] H. Calcutt[4,5], E.F. van Dishoeck[2,6], H. Linnartz[7], J.K. Jørgensen[8], R.T. Garrod[9], and J. Bouwman[7]

[1] Physics Institute, University of Bern, Sidlerstrasse 5, 3012 Bern, Switzerland
e-mail: niels.ligterink@csh.unibe.ch
[2] Leiden Observatory, Leiden University, PO Box 9513, 2300 RA Leiden, The Netherlands
[3] Laboratoire d'Astrophysique de Bordeaux, Univ. Bordeaux, CNRS, B18N, allée Geoffroy Saint-Hilaire, 33615 Pessac, France
[4] Department of Space, Earth and Environment, Chalmers University of Technology, 41296, Gothenburg, Sweden
[5] Institute of Astronomy, Faculty of Physics, Astronomy and Informatics, Nicolaus Copernicus University, Grudziadzka 5, 87-100 Torun, Poland
[6] Max-Planck Institut für Extraterrestrische Physik (MPE), Giessenbachstr. 1, 85748 Garching, Germany
[7] Laboratory for Astrophysics, Leiden Observatory, Leiden University, PO Box 9513, 2300 RA Leiden, The Netherlands
[8] Centre for Star and Planet Formation, Niels Bohr Institute & Natural History Museum of Denmark, University of Copenhagen, Øster Voldgade 5–7, 1350 Copenhagen K., Denmark
[9] Departments of Chemistry and Astronomy, University of Virginia, Charlottesville, VA 22904, USA

Received October 8, 2020; accepted December 22, 2020

ABSTRACT

Aims. Methyl isocyanate (CH_3NCO) and glycolonitrile ($HOCH_2CN$) are isomers and prebiotic molecules that are involved in the formation of peptide structures and the nucleobase adenine, respectively. These two species are investigated to study the interstellar chemistry of cyanides (CN) and isocyanates (NCO) and to gain insight into the reservoir of interstellar prebiotic molecules.
Methods. ALMA observations of the intermediate-mass Class 0 protostar Serpens SMM1-a and ALMA-PILS data of the low-mass Class 0 protostar IRAS 16293B are used. Spectra are analysed with the CASSIS line analysis software package in order to identify and characterise molecules.
Results. CH_3NCO, $HOCH_2CN$, and various other molecules are detected towards SMM1-a. $HOCH_2CN$ is identified in the PILS data towards IRAS 16293B in a spectrum extracted at a half-beam offset position from the peak continuum. CH_3NCO and $HOCH_2CN$ are equally abundant in SMM1-a at [X]/[CH_3OH] of 5.3×10^{-4} and 6.2×10^{-4}, respectively. A comparison between SMM1-a and IRAS 16293B shows that $HOCH_2CN$ and HNCO are more abundant in the former source, but CH_3NCO abundances do not differ significantly. Data from other sources are used to show that the [CH_3NCO]/[HNCO] ratio is similar in all these sources within ~10%.
Conclusions. The new detections of CH_3NCO and $HOCH_2CN$ are additional evidence for a large interstellar reservoir of prebiotic molecules that can contribute to the formation of biomolecules on terrestrial planets. The equal abundances of these molecules in SMM1-a indicate that their formation is driven by kinetic processes instead of thermodynamic equilibrium, which would drive the chemistry to one product. $HOCH_2CN$ is found to be much more abundant in SMM1-a than in IRAS 16293B. From the observational data, it is difficult to indicate a formation pathway for $HOCH_2CN$, but the thermal Strecker-like reaction of CN^- with H_2CO is a possibility. The similar [CH_3NCO]/[HNCO] ratios found in the available sample of studied interstellar sources indicate that these two species either are chemically related or their formation is affected by physical conditions in the same way. Both species likely form early during star-formation, presumably via ice mantle reactions taking place in the dark cloud or when ice mantles are being heated in the hot core. The relatively high abundances of $HOCH_2CN$ and HNCO in SMM1-a may be explained by a prolonged stage of relatively warm ice mantles, where thermal and energetic processing of HCN in the ice results in the efficient formation of both species.

Key words. Astrochemistry – Astrobiology – Individual Objects: Serpens SMM1 – ISM: abundances – Submillimeter: ISM

1. Introduction

Observations of molecules towards star-forming regions give insight into the kind of species that end up in planet-forming discs. These molecules not only aid planet formation but can also seed newly formed planets with a cocktail of molecules from which larger organic molecules can be formed. Prebiotic molecules are of particular interest, as they are involved in the formation of biomolecules, such as amino acids, nucleobases, proteins, and lipids (Sandford et al. 2020). In the interstellar medium (ISM) and on planets, prebiotic molecules are the building blocks from which biomolecules are made.

In the ISM, several prebiotic molecules have been detected. Examples are formamide (NH_2CHO, Rubin et al. 1971) a precursor to nucleobases and amino acids (Saladino et al. 2012), the simplest sugar-like molecule glycolaldehyde ($HOCH_2CHO$, Hollis et al. 2000; Jørgensen et al. 2012), methylamine (CH_3NH_2, Kaifu et al. 1974; Bøgelund et al. 2019) and aminoacetonitrile (NH_2CH_2CN, Belloche et al. 2008), building blocks of the amino acid glycine (Holtom et al. 2005; Lee et al. 2009), the peptide building blocks acetamide ($CH_3C(O)NH_2$)

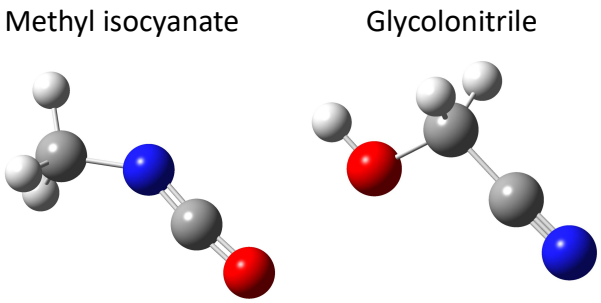


Fig. (1) Structures of the C_2H_3NO isomers methyl isocyanate (CH_3NCO, left) and glycolonitrile ($HOCH_2CN$, right).

and N-methylformamide (CH_3NHCHO, Hollis et al. 2006; Halfen et al. 2011; Belloche et al. 2017, 2019; Ligterink et al. 2020), the chiral molecule propylene oxide (CH_3CHCH_2O, McGuire et al. 2016), cyanomethanimine (NHCHCN), which can oligomerise to form adenine (Zaleski et al. 2013; Rivilla et al. 2019), and the nucleobase precursors cyanamide (NH_2CN, Turner et al. 1975; Coutens et al. 2018), hydroxylamine (NH_2OH, Rivilla et al. 2020) and carbamide (also known as urea, $NH_2C(O)NH_2$, Belloche et al. 2019). Over the past years, methyl isocyanate (CH_3NCO, Halfen et al. 2015; Cernicharo et al. 2016; Ligterink et al. 2017) has been detected in several interstellar sources and recently its isomer glycolonitrile (also known as hydroxy acetonitrile, $HOCH_2CN$, Zeng et al. 2019) was identified for the first time in the ISM towards the low-mass protostar IRAS 16293–2422B (hereafter IRAS 16293B). Both these isomers are prebiotic molecules. CH_3NCO can engage in reactions that form peptide-like structures, while $HOCH_2CN$ is known to accelerate the oligomerisation of HCN in liquids and ice under terrestrial conditions, forming the nucleobase adenine (Schwartz & Goverde 1982; Schwartz et al. 1982).

Besides their relevance to prebiotic chemistry, CH_3NCO and $HOCH_2CN$ are also interesting molecules to gain insight into interstellar nitrogen chemistry. While these molecules, being isomers, have the same elemental composition (C_2H_3NO), their chemical structures differ significantly, see Fig. 1. Recent quantum chemical calculations of the stability of C_2H_3NO isomers in general, also reveal that CH_3NCO is the most stable species of those, followed by $HOCH_2CN$ (Fourré et al. 2020). Therefore, observations of this isomer couple provide information on interstellar reactions involving cyanides (-CN) and isocyanates (-NCO), two important nitrogen-bearing chemical groups, and the physical conditions that steer or prohibit this chemistry.

After the first detection of CH_3NCO (Halfen et al. 2015; Cernicharo et al. 2016), HNCO was suggested to be involved in its formation due to their structural similarity and the large HNCO abundances in interstellar gas and ice (in the form of OCN^- Boogert et al. 2015). Various gas-phase and solid-state methylation (the addition of a CH_3 functional group to a molecule) reactions of HNCO, the OCN radical, and the OCN^- anion have been proposed as possible reaction pathways. Experimental investigations (Ligterink et al. 2017; Maté et al. 2018) and modeling studies (Martín-Doménech et al. 2017; Quénard et al. 2018; Majumdar et al. 2018) indicate solid-state methylation in the ice mantle as the main pathway to form CH_3NCO:

$$CH_3 + NCO \longrightarrow CH_3NCO \cdot \quad (1)$$

Variations of this pathway, such as the methylation of HNCO or OCN^- may be possible as well, while completely different reactions, such as the hydrogenation of HCN...CO may form CH_3NCO as well.

No gas-phase formation pathways are known for glycolonitrile, but solid-state production routes have been studied theoretically (Woon 2001) and experimentally (Danger et al. 2012, 2014). Laboratory work indicates that the thermally activated reaction between a cyanide anion (CN^-) and formaldehyde (H_2CO) forms $HOCH_2CN$:

$$[XH^+CN^-] + H_2CO \longrightarrow HOCH_2CN + X, \quad (2)$$

where X is a molecule that can act as a base, such as ammonia (NH_3) or water (H_2O). This reaction is the solid-state equivalent of the Strecker synthesis, which is a sequence of chemical reactions that produce amino acids. The Strecker-like formation of $HOCH_2CN$ is linked to the formation of aminomethanol ($HOCH_2NH_2$, Bossa et al. 2009) and aminoacetonitrile (NH_2CH_2CN, Danger et al. 2011). The latter of these species is detected in the ISM and known as a possible intermediate in the formation of the amino acid glycine (Belloche et al. 2008). Irradiation of $HOCH_2CN$ results in the photoproducts formylcyanide (HC(O)CN) and ketenimine (CH_2CNH). Although not investigated, hydrogenation and oxygen additions of these two species may provide pathways to form $HOCH_2CN$ in the ISM. The solid-state radical-radical reactions HO + CH_2CN and $HOCH_2$ + CN can also form glycolonitrile, but neither of these reactions has been investigated (Margulès et al. 2017). However, precursor species to these reactions can be present in ice mantles, in particular when methanol (CH_3OH) or acetonitrile (CH_3CN) are energetically processed (Allamandola et al. 1988; Hudson & Moore 2004; Bulak et al. 2020).

Methyl isocyanate and glycolonitrile can thus be used as tracers of reactions involving CN and NCO and investigating their interstellar abundances reveals information about the chemical and physical processes that drive these reactions and interstellar nitrogen chemistry as a whole. CH_3NCO and $HOCH_2CN$ have only been detected simultaneously in the low-mass protostar IRAS 16293B (Ligterink et al. 2017; Martín-Doménech et al. 2017; Zeng et al. 2019), albeit in different observational data sets. Due to this limited sample size, it is difficult to derive correlations or variations in the C_2H_3NO isomer chemistry and therefore simultaneous identifications in other sources are required. Here, deep ALMA observations of the intermediate-mass Class 0 protostar Serpens SMM1-a (hereafter SMM1-a) are presented to derive additional constraints on CH_3NCO and $HOCH_2CN$ chemistry.

The Serpens star-forming region contains multiple deeply embedded sources, of which SMM1 is the brightest (Casali et al. 1993). The Serpens region contains multiple outflows and jets, some of which originate from SMM1 (Dionatos et al. 2013; Hull et al. 2016). The chemistry of the SMM1 hot corino, its outflows, and the Serpens core have been characterised in various studies (e.g., White et al. 1995; Hogerheijde et al. 1999; Kristensen et al. 2010; Öberg et al. 2011; Goicoechea et al. 2012; Tychoniec et al. 2019). High-resolution continuum jet observations have shown that SMM1 consists of multiple sources, of which SMM1-a is the main one (Choi 2009; Dionatos et al. 2014; Hull et al. 2017). SMM1-a has SMM1-b as a close neighbor at ~500 au, while two other sources, SMM1-c and -d, are located further away to its north. Recent distance measurements place the Serpens core, and therefore SMM1, at a distance of 436.0±10 pc (Ortiz-León et al. 2017), resulting in a luminosity estimate of the entire SMM1 source of ~100 $L_\odot$. SMM1-a is considered to

be an intermediate-mass protostar (Hull et al. 2017; Tychoniec et al. 2019).

In this work, the detection and analysis of the isomers $HOCH_2CN$ and CH_3NCO towards SMM1-a are presented and compared with literature results of IRAS 16293B and those of other sources. In section 2 the observations towards SMM1 and the analysis method are presented. The detections of $HOCH_2CN$, CH_3NCO, and various other molecules are presented in section 3. Section 4 discusses these detections and their likely formation pathways. The conclusions of this work are presented in section 5.

2. Data & Methods

2.1. Observations and spectra of Serpens SMM1

SMM1 was observed on 27-March-2019 during ALMA cycle 6, as part of project #2018.1.00836.S (PI: N.F.W. Ligterink). The region was observed using a total of 42 antennae with baselines spanning 15 – 332 meters in configuration C43-5. The on-source integration time was 50 minutes, towards the phase centre α_{J2000} = 18:29:49.80 δ_{J2000} = +01:15:20.6. Spectra were recorded in select frequency windows between 217.59 and 235.93 GHz, at resolutions of 488.21 kHz (0.33 km s^{-2}) and 1952.84 kHz (1.25 km s^{-2}) for the continuum window, see Table 1. The data were calibrated and imaged with version 5.4.0-70 of the Common Astronomy Software Applications (CASA). Bandpass and flux calibration was conducted on J2000–1748, while phase calibration was performed on J1851+0035. The flux uncertainty was ≤20%. To reach the desired sensitivity, the measurement sets were cleaned using the Hogbom algorithm (Högbom 1974) and Briggs weighting with a robust parameter of 0.5. This resulted in an angular resolution of 1″.32×1″.04 and an rms noise of 2.6 mJy beam^{-1} km s^{-1} in the final spectral data cubes. The primary beam of the observations was 26″.

Table (1) Frequency settings of ALMA SMM1 observations

Frequency range (GHz)	Bandwidth (GHz)	Resolution (kHz)	Resolution (km s^{-1})
217.59 – 217.70	0.117	488.21	0.33
217.97 – 218.09	0.117	488.21	0.33
218.43 – 218.55	0.117	488.21	0.33
218.92 – 219.03	0.117	488.21	0.33
219.71 – 219.82	0.117	488.21	0.33
221.30 – 221.42	0.117	488.21	0.33
221.42 – 221.53	0.117	488.21	0.33
221.53 – 221.65	0.117	488.21	0.33
231.74 – 231.97	0.234	488.21	0.33
233.41 – 233.65	0.234	488.21	0.33
234.06 – 235.93	1.875	1952.84	1.25

Due to the line-richness of the source, the following procedure was followed to properly subtract the continuum from the line observations. We imaged all spectral windows without the continuum removed and used the corrected sigma-clipping method of the STATCONT package[1] (Sánchez-Monge et al. 2018) to extract a continuum-subtracted line cube. STATCONT can only subtract zeroth-order polynomials, while in this dataset non-zeroth-order baselines are visible. Furthermore, continuum subtraction in the uv-plane is more desirable since the deconvolution of the line emission is more robust when it is not subjected to the deconvolution errors of the brighter continuum. Therefore, the STATCONT outputs were used to identify the line-free channels in the spectra and the continuum was subtracted in the uv-plane with the *uvcontsub* task in CASA. Line-free channels are sparse, but for most spectral windows, at least 20% of the bandwidth was given as input to the *uvcontsub* task, with the exception of two spectral windows, where only 10% of the bandwidth was line-free. From the resulting datacube, the SMM1-a hot core spectrum was extracted towards the peak continuum position α_{J2000} = 18:29:49.793, δ_{J2000} = +1.15.20.200. From the average continuum flux density (0.41 mJy beam^{-1}), the background temperature was determined to be ∼5.2 K.

[1] https://hera.ph1.uni-koeln.de/~sanchez/statcont

2.2. PILS observations and spectra of IRAS 16293B

In this work, the column density of $HOCH_2CN$ is determined independently from the detection presented by (Zeng et al. 2019) by analysing data from the Protostellar Interferometric Line Survey (PILS). Other species relevant to this work are also searched for in the PILS data set. The observational details of the PILS survey have been presented in various other publications (e.g., Jørgensen et al. 2016) and here only the most relevant information is presented. In short, the PILS survey makes use of ALMA band 7 observations, covering a frequency range from 329 to 363 GHz at a spatial resolution of 0″.5. To investigate the chemical inventory of IRAS 16293B, spectra are extracted at several positions. These positions are on the peak continuum, a half-beam offset from the peak continuum, and a full-beam offset from the peak continuum. Most PILS analyses of IRAS 16293B make use of the spectrum at the full-beam offset position Jørgensen et al. (e.g., 2016); Coutens et al. (e.g., 2016); Ligterink et al. (e.g., 2017); Coutens et al. (e.g., 2018); Persson et al. (e.g., 2018); Calcutt et al. (e.g., 2018); Jørgensen et al. (e.g., 2018). In this work, this is the main position for which molecular ratios with $HOCH_2CN$ are determined, but the spectra of other positions are also analysed. The systemic velocity towards these positions is V_{LSR} = 2.7 km s^{-1} and the line width is approximately ΔV = 1.0 km s^{-1}. Due to the dense dust around IRAS 16293B, the background temperatures (T_{BG}) at these positions are higher than the cosmic microwave background radiation temperature of 2.7 K and couple with the molecular line emission (see Ligterink et al. 2018). At the full-beam offset position T_{BG} = 21 K, while at the half-beam offset position it is T_{BG} = 52 K.

2.3. Analysis method

The spectra were analyzed with the CASSIS[2] line analysis software. Spectral line lists were obtained from the JPL database for molecular spectroscopy (Pickett et al. 1998), the Cologne Database for Molecular Spectroscopy (CDMS, Müller et al. 2001, 2005), and from literature. An overview of the spectroscopic line lists used in this work and the laboratory works they are based on is given in Appendix A. Given a spectroscopic line list as input, CASSIS can produce synthetic spectra of a molecule based on parameters such as column density (N_T), excitation temperature (T_{ex}), peak gas velocity (V_{LSR}), line width at half maximum (ΔV), and source size (θ_{source}). These parameters were given as free parameters to a Monte-Carlo Markov Chain (MCMC) algorithm and χ^2 minimisation routine. This routine finds the best-fit of a synthetic spectrum to an observed spectrum over a specified parameter space, thereby determining the

[2] CASSIS has been developed by IRAP-UPS/CNRS (http://cassis.irap.omp.eu)

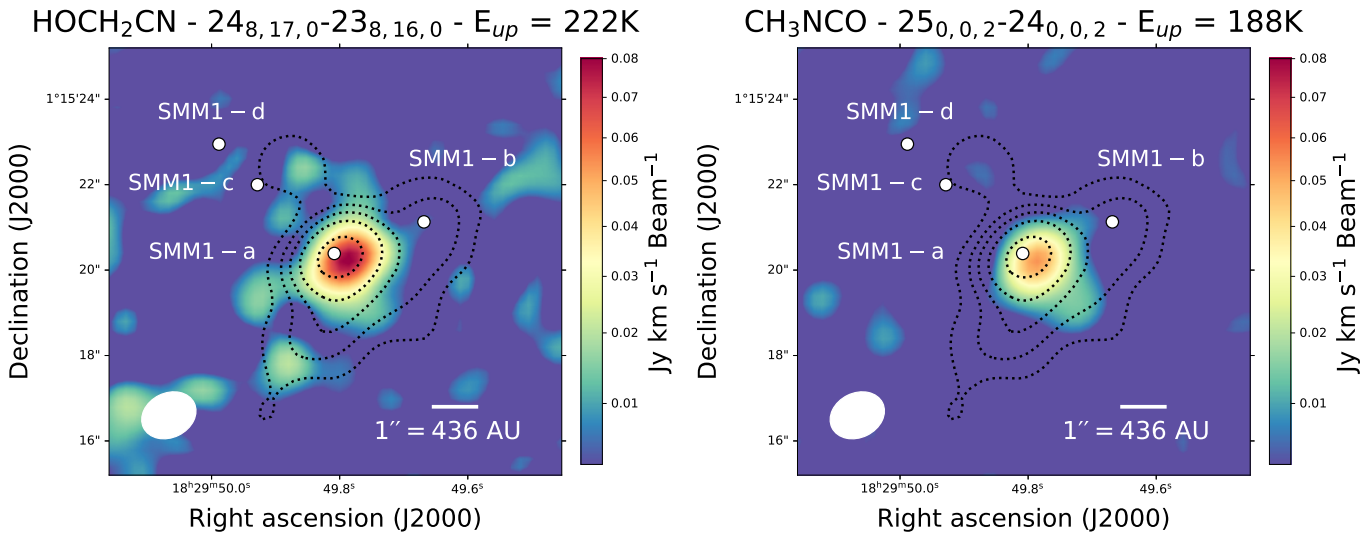


Fig. (2) Moment 0 maps of the $HOCH_2CN$ $24_{8,17/16}$–$23_{8,16/15}$, E_{up} = 222 K line and the CH_3NCO ν=0 $25_{0,0}$–$24_{0,0}$, E_{up} = 188 K line towards SMM1. Both lines are integrated over 8 velocity bins, centered on the peak frequency of each line as determined towards SMM1-a. Positions of protostars in the SMM1 region are indicated and the beam size (1.″32×1.″04) is visualised in the bottom left corner. Dust continuum contours are given by the black dotted line at the levels of 0.02, 0.05, 0.1, 0.2, 0.5 Jy Beam^{-1}.

Table (2) Best-fit parameters for molecules detected towards SMM1-a in a 1.″2 beam.

Molecule	Lines #	N_T (cm^{-2})	T_{ex} (K)	V_{LSR} km s^{-1}	ΔV km s^{-1}	[X] / [CH_3OH]	[X] / [HNCO]
$HOCH_2CN$	18	(7.4±0.9)×10^{14}	260±45	6.8±0.2	2.5±0.3	6.2×10^{-4}	7.4×10^{-2}
CH_3NCO	12	(6.4±1.9)×10^{14}	240±60	7.0±0.4	3.0±0.6	5.3×10^{-4}	6.4×10^{-2}
D_2CO	3	(5.4±2.5)×10^{14}	[200]	7.4±0.4	3.9±0.2	4.5×10^{-4}	5.4×10^{-2}
$CH_3^{18}OH$	4	(2.0±1.1)×10^{15}	250±60	7.1±0.2	2.8±0.3	–	–
$^{12}CH_3OH^a$	5^b	1.1×10^{18}	–	–	–	1.0	110
CH_3CN^c	6	(1.3±0.3)×10^{15}	190±25	7.5±0.2	3.4±0.3	1.1×10^{-3}	0.1
NH_2CN	3	(5.1±1.3)×10^{13}	190±40	7.1±0.2	3.2±0.4	4.3×10^{-5}	5.1×10^{-3}
$HN^{13}CO$	3	(1.9±0.3)×10^{14}	190±30	7.6±0.2	3.5±0.3	–	–
$HN^{12}CO^a$	5^b	1.0×10^{16}	–	–	–	1.1×10^{-2}	1.0
CH_3CH_2OH	14	(4.1±0.9)×10^{15}	210±25	7.3±0.2	2.8±0.6	4.1×10^{-3}	0.3
CH_3OCHO	24	(7.4±0.7)×10^{15}	215±20	7.3±0.2	3.1±0.3	7.4×10^{-3}	0.6
a-$(CH_2OH)_2$	14	(1.7±0.5)×10^{15}	195±70	7.2±0.2	2.7±0.3	1.7×10^{-3}	0.1
CH_3CNO	0	≤1.0×10^{13}	[200]	[7.0]	[3.5]	≤9.1×10^{-6}	≤1.0×10^{-3}
CH_3OCN	0	≤5.0×10^{13}	[200]	[7.0]	[3.5]	≤4.6×10^{-6}	≤5.0×10^{-3}
CH_2CNH	0	≤1.0×10^{15}	[200]	[7.0]	[3.5]	≤8.3×10^{-4}	0.1
CH(O)CN	0	≤2.0×10^{14}	[200]	[7.0]	[3.5]	≤1.7×10^{-4}	≤2.0×10^{-2}
NH_2CH_2CN	0	≤1.0×10^{14}	[200]	[7.0]	[3.5]	≤8.3×10^{-5}	≤1.0×10^{-2}

Notes. Values in brackets are assumed. ^{a}Main isotopologue column densities are determined by applying the ratios $^{16}O/^{18}O$ = 560 and $^{12}C/^{13}C$ = 52.5 to the minor isotopologue column densities. ^{b}The number of lines identified of the main isotopologue in this data set. ^{c}The CH_3CN best-fit parameters are determined from its vibrationally excited state ν_8=1.

best-fit parameters and thus column density and excitation temperature of a molecule. For the analysis, optically thin lines ($\tau \ll 1.0$) were used. The τ-value was approximated from the by-eye synthetic fit (see below) of the observed rotational lines with the CASSIS software. The molecules were assumed to be in local thermodynamic equilibrium (LTE). Errors on physical parameters take the uncertainty of the fit and the flux uncertainty as input and are calculated from the spread in χ^2 values around the minimum to a 3σ confidence level.

In this work, spectral lines of a molecule were identified in the observed spectra and a by-eye synthetic fit of the lines was made. For the by-eye fit, line width and peak velocity are determined from prominent spectral lines of molecules such as HNCO and CH_3OH and used as a first approximation for other molecules. An excitation temperature of 200 K is taken as an initial guess and followed by a round of adjusting column density and rotational temperature until a reasonable by-eye fit was found. The by-eye fit results were given as starting parameters for the MCMC χ^2 minimisation routine. The χ^2 minimisation was performed on lines that are not blended and have minimal contributions from the wings of neighboring lines. Blending species were identified by checking the line position for other lines of known hot core / corino species with $A_{ij} > 1\times10^{-6}$ and E_{up} of 0–1000 K. The column density was given as a free parameter over two orders of magnitude centered on the by-eye fit column density and the excitation temperature was a free parameter

Table (3) Best-fit parameters of $HOCH_2CN$ and related species towards IRAS 16923B in the PILS data set in a 0″.5 beam

Molecule	N_T (cm^{-2})	T_{ex} (K)	[X] / [CH_3OH][a]	[X] / [HNCO][a]
$HOCH_2CN$	≤1.0×10^{15}	[150]	≤1.0×10^{-4}	≤3.3×10^{-2}
$HOCH_2CN$	≤1.0×10^{15}	[300]	≤1.0×10^{-4}	≤3.3×10^{-2}
CH_2CNH	≤1.0×10^{15}	[100]	≤1.0×10^{-4}	≤3.3×10^{-2}
CH_2CNH	≤2.0×10^{15}	[300]	≤2.0×10^{-4}	≤6.7×10^{-2}
CH(O)CN	≤5.0×10^{14}	[100]	≤5.0×10^{-5}	≤1.7×10^{-2}
CH(O)CN	≤5.0×10^{14}	[300]	≤5.0×10^{-5}	≤1.7×10^{-2}
NH_2CH_2CN	≤1.0×10^{15}	[100]	≤1.0×10^{-4}	≤3.3×10^{-2}
NH_2CH_2CN	≤5.0×10^{14}	[300]	≤5.0×10^{-5}	≤1.7×10^{-2}

Notes. Values in brackets are assumed. V_{LSR} = 2.7 km s^{-1} and ΔV = 1.0 km s^{-1}. Note that some upper limit column densities are similar because the upper state energies of the lines cover only a narrow range of energies. [a]CH_3OH and HNCO column densities were adopted from Jørgensen et al. (2018) and Coutens et al. (2016), respectively.

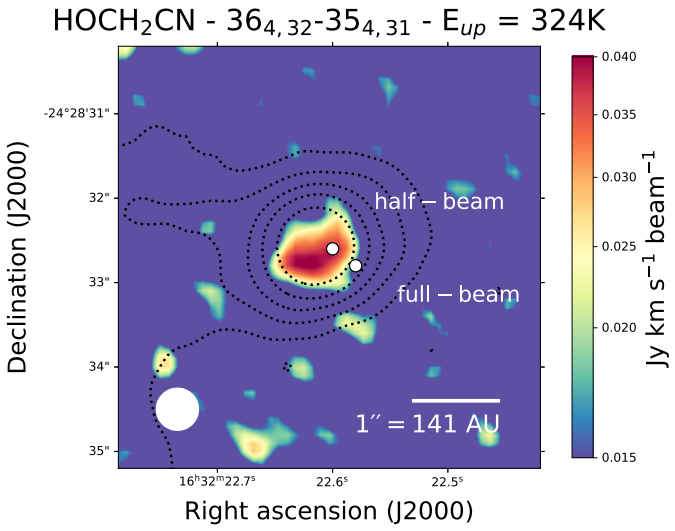


Fig. (3) Moment 0 map of the $HOCH_2CN$ $36_{4,32}$–$35_{4,31}$, E_{up} = 324 K line towards IRAS 16293B. The line is integrated over 8 velocity bins, centered on the peak frequency of the line. The positions of the half-beam and full-beam offset positions around IRAS 16293B are indicated and the beam size (0″.5×0″.5) is visualised in the bottom left corner. Dust continuum contours are given by the black dotted line at the levels of 0.02, 0.05, 0.1, 0.2, 0.5 Jy Beam^{-1}.

from 50 – 350 K. For SMM1-a, ΔV was a free parameter from 1.0 – 4.0 km s^{-1}, and the source velocity was a free parameter between 6.0 – 9.0 km s^{-1}. The source size was assumed to be equal to the beam size and taken to be 1″.2, resulting in a beam filling factor of 0.5. A background continuum temperature (T_{bg}) of 5.2 K was used.

For the analysis of IRAS 16293B, ΔV and V_{LSR} were fixed to 1.0 km s^{-1} and 2.7 km s^{-1}, respectively. The source size was assumed to be equal to the beam size at 0″.5, while a background continuum temperature of T_{bg} = 21 K was used.

3. Results

3.1. SMM1

In the spectra of SMM1-a, multiple unblended rotational lines of the isomers $HOCH_2CN$ and CH_3NCO v=0 are found. Moment 0 maps (the spatial mapping of the integrated line intensity of a single rotational line) of both species show that most emission originates from SMM1-a, see Fig. 2. The identified lines towards SMM1-a are presented in Figs. 4 and 5. For $HOCH_2CN$, this is the second independent interstellar detection of this molecule (the first detection of $HOCH_2CN$ was presented towards IRAS 16293B by Zeng et al. 2019), while the first detection of CH_3NCO towards SMM1-a is part of only a handful of detections of this species towards other interstellar sources.

Several other species are identified in the SMM1-a spectra as well. Rotational lines of acetonitrile (CH_3CN v_8=1), cyanamide (NH_2CN), ethanol (CH_3CH_2OH), the anti-conformer of ethylene glycol (a-($CH_2OH)_2$), deuterated formaldehyde (D_2CO), isocyanic acid (HN^{12}CO and HN^{13}CO), methylformate (CH_3OCHO), and methanol ($^{12}CH_3OH$ and $CH_3^{18}OH$) are detected. Rotational lines of the C_2H_3NO isomers methyl fulmiate (CH_3CNO) and methyl cyanate (CH_3OCN) were not identified in the spectra. The molecules aminoacetonitrile (NH_2CH_2CN), ketenimine (CH_2CNH), and formylcyanide (HC(O)CN) are searched for, but not identified. Spectra are presented in Appendix B and spectroscopic parameters of transitions are provided in Table 5. Following the procedure detailed in Sect. 2.3, the best-fit parameters of these species are determined. For undetected species, upper limit column densities are determined by assuming T_{ex} = 200 K, which is chosen as a representative excitation temperature from the molecules that are detected. The fit parameters are presented in Table 2. The main isotopologues of CH_3OH and HNCO are optically thick and their column densities are therefore determined from minor isotopologues. This is done by multiplying with the local interstellar $^{12}C/^{13}C$ ratio of 52.5±15.4 (Yan et al. 2019) and $^{16}O/^{18}O$ ratio of 560 (Wilson 1999).

3.2. IRAS 16293B

Because the chemical inventory of IRAS 16293B is well characterised with results from the PILS survey, this data set is used to search for $HOCH_2CN$ and related species to make an unbiased chemical comparison with SMM1-a. While $HOCH_2CN$ was identified towards IRAS 16293B by Zeng et al. (2019), this detection cannot be confirmed in the PILS spectrum at the full-beam offset position (the position commonly used for the molecular analysis of IRAS 16293B with PILS data, see Fig.3). Figure 6 shows the $HOCH_2CN$ a-type transitions ($J'_{0,J'} - J''_{0,J''}$) at this position covered by the PILS spectral range with a synthetic glycolonitrile spectrum at N_T = 1.0×10^{15} cm^{-2} and T_{ex} = 150 and 300 K. A synthetic spectrum of the previously identified molecules towards IRAS 16293B at the full-beam offset

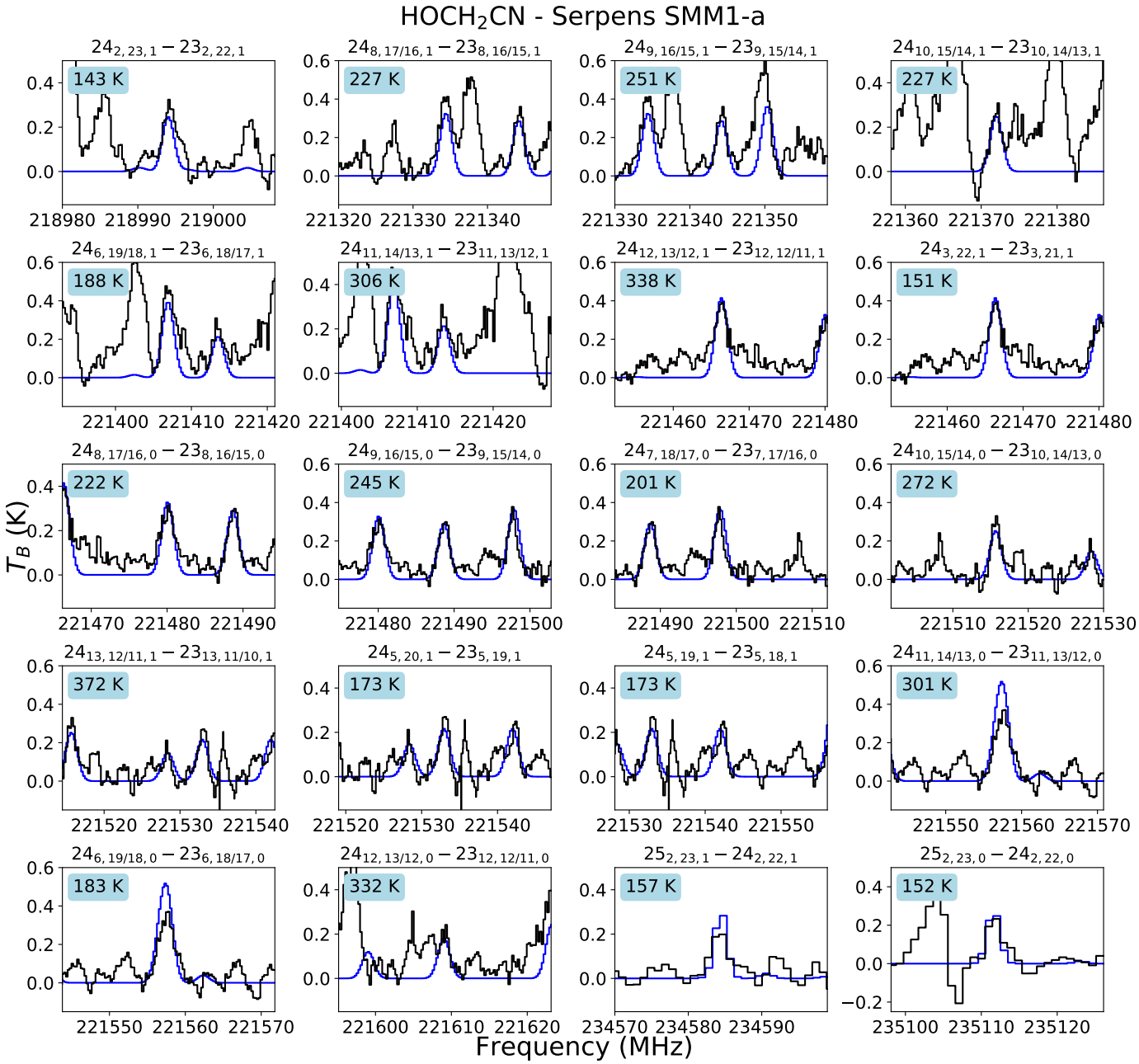


Fig. (4) Identified lines of $HOCH_2CN$ towards SMM1. The observed spectrum is plotted in black, with the best-fit synthetic spectrum overplotted in blue (N_T = (7.4±0.9)×10^{14} cm^{-2}, T_{ex} = 260±45 K). The transition is indicated at the top of each panel and the upper state energy is given in the top left of each panel.

position is added in green. Note that this synthetic spectrum only includes molecules listed in previous publications and does not include $HOCH_2CN$. The molecules and parameters used in this fit are listed in Table 5. When a rotational spectrum is experimentally measured, a-type transitions are usually the first and most accurately determined transitions. The assignment of these a-type transitions, therefore, is key to claim an unambiguous identification. However, of the seven a-type transitions covered by the PILS survey, only the $39_{0,39,1} - 38_{0,38,1}$ transition at 344625 MHz is possibly detected, although this feature has a contribution of a HONO and CH_2DOH transition (Jørgensen et al. 2016, 2018; Coutens et al. 2019), which also can fully reproduce this line. Appendix C presents all the $HOCH_2CN$ transitions at the full-beam offset position that are largely unblended and have $A_{ij} \geq 1\times10^{-3}$ s^{-1}. At the full-beam offset position, a large number (∼40) of glycolonitrile transitions that are present in the synthetic spectrum are not seen in the observed spectrum. We note that due to the line-richness of the source the baseline subtraction is challenging and in some cases, it can be oversubtracted. This can explain why certain $HOCH_2CN$ lines are not clearly observed, as the baseline at these positions dips. Furthermore, some transitions seem to be better reproduced with low excitation temperatures, whereas others require warmer temperatures. This could indicate that two gas components are traced, as also shown by Zeng et al. (2019), but at this position these components are hard to distinguish. Therefore, $HOCH_2CN$ can only tentatively be identified towards the full-beam offset posi-

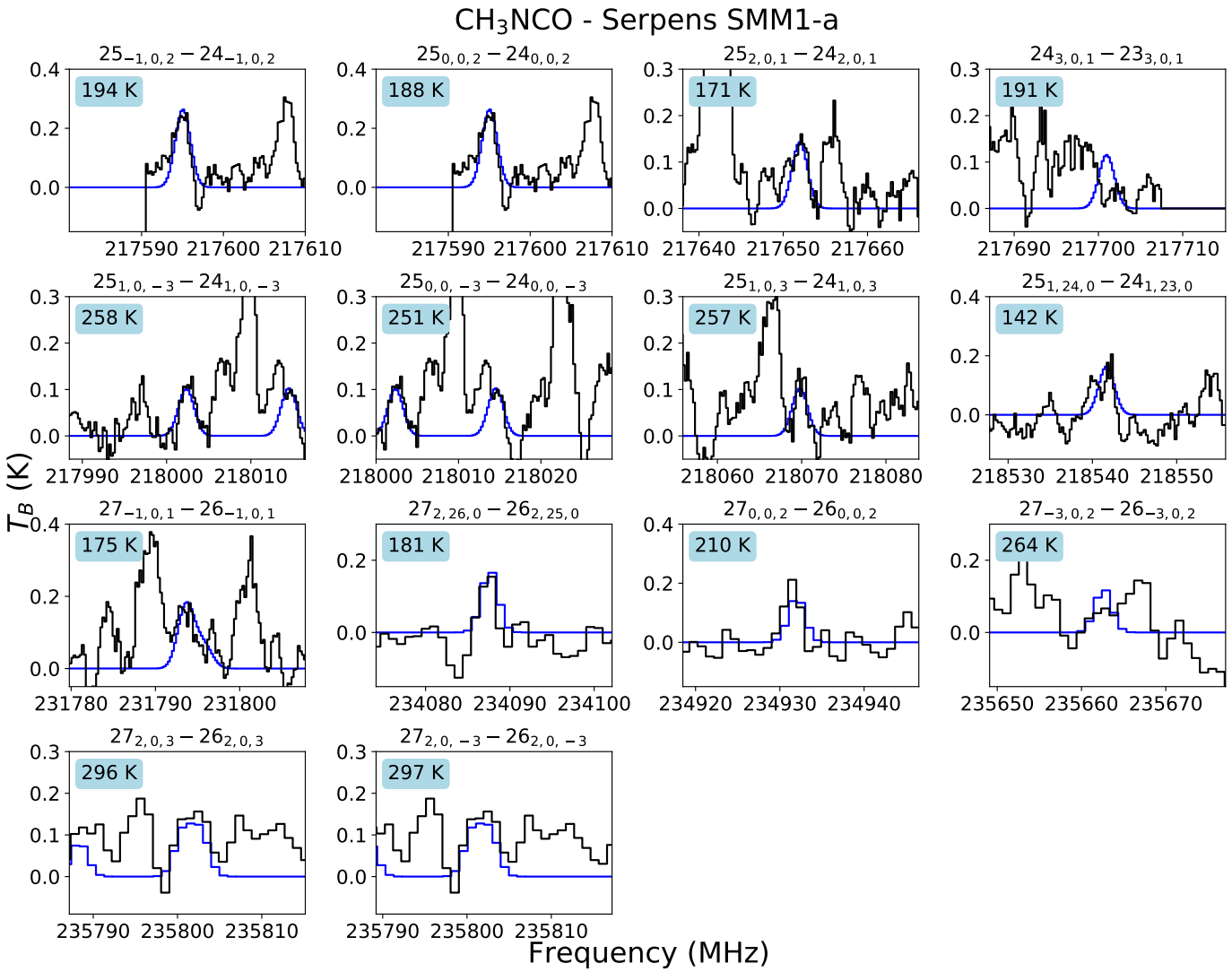


Fig. (5) Identified lines of CH_3NCO, v=0 towards SMM1. The observed spectrum is plotted in black, with the best-fit synthetic spectrum overplotted in blue (N_T = (6.4±1.9)×10^{14} cm^{-2}, T_{ex} = 240±60 K). The transition is indicated at the top of each panel and the upper state energy is given in the top left of each panel.

tion, with a column density of ∼1.0×10^{15} cm^{-2} at T_{ex} = 150 and 300 K.

At the half-beam offset position (see Fig. 3), which is closer to the continuum peak of IRAS 16293B, $HOCH_2CN$ can be identified. At this position, at least four a-type transitions are clearly detected, while the three other lines suffer from line blending or absorption features, see Fig. 7. These lines can approximately be fitted with synthetic spectra of N_T = 3.0×10^{15} cm^{-2} for T_{ex} = 150 and 300 K. In appendix C the remaining $HOCH_2CN$ transitions at the half-beam offset position are shown, with the same selection criteria for the full-beam offset position.

In Fig. 3 the moment 0 map of the $HOCH_2CN$ $36_{4,32}$–$35_{4,31}$ transition towards IRAS 16293B is shown. This map shows that $HOCH_2CN$ emission towards IRAS 16293B is compact. This explains the non-detection of glycolonitrile towards the full-beam offset position, as this position misses most of the $HOCH_2CN$ emission. At the same time, this map demonstrates why Zeng et al. (2019) could detect $HOCH_2CN$ towards IRAS 16293B, since these authors use a larger observational beam of 1.″6 beam (with an assumed source size of 0.″5), which covers the entire emitting area.

Because the chemical inventory at the full-beam offset position of the PILS data is best characterised, the tentative detection of $HOCH_2CN$ towards this position, with a column density of ∼1.0×10^{15} cm^{-2}), is used for further analysis in this paper. However, the identification of $HOCH_2CN$ towards the half-beam offset position in combination with the moment 0 map support the detection of $HOCH_2CN$ towards IRAS 16923B by Zeng et al. (2019).

The related species CH_2CNH, CH(O)CN, and NH_2CH_2CN are also searched for in the PILS dataset, but clear and unblended lines are not identified. For these species upper limit column densities are determined at the full-beam offset position at excitation temperatures of 100 and 300 K. The upper limit column densities and abundances of all species are presented in Table 3.

4. Discussion

In this work, several molecules are detected towards SMM1-a and analysed. Most notable are the detection of the C_2H_3NO isomers CH_3NCO (methyl isocyanate) and $HOCH_2CN$ (glycolonitrile). For $HOCH_2CN$, this is only its second interstellar detec-

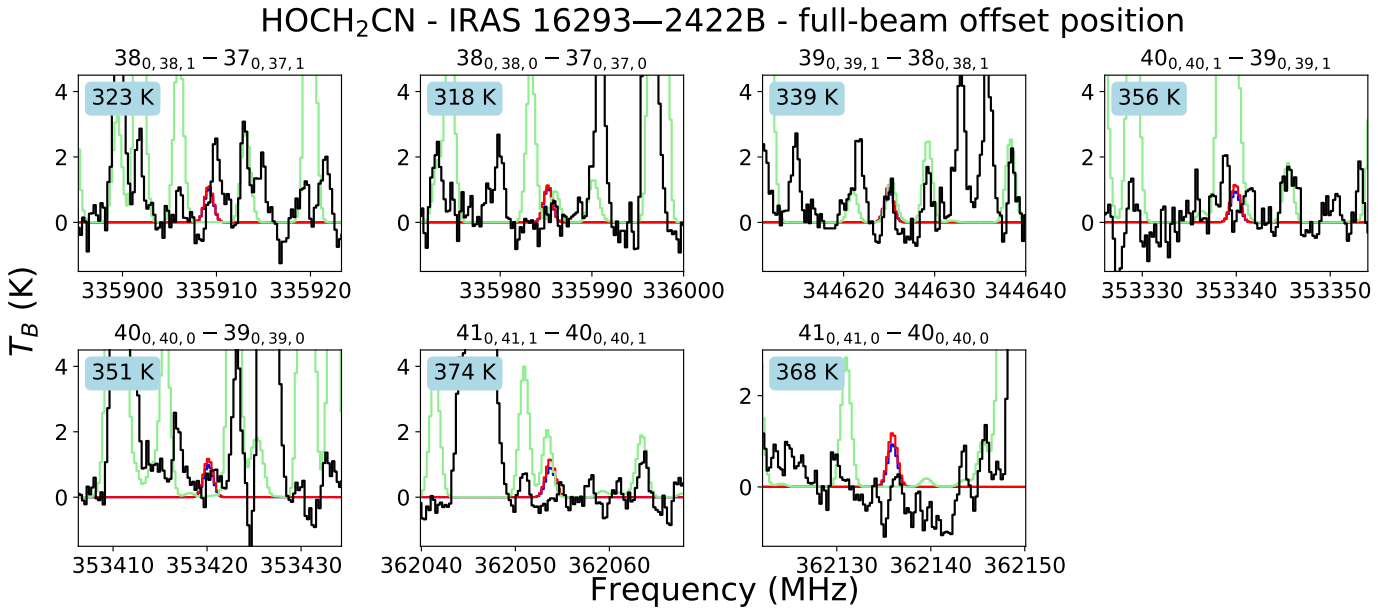


Fig. (6) Overview of a-type ($J'_{0,J'} - J''_{0,J''}$) $HOCH_2CN$ transitions covered by the PILS spectrum towards the full-beam offset position of IRAS 16293B, illustrating the non-detection of these lines in this spectrum. The observed spectrum is plotted in black and synthetic spectra for a column density of $1.0{\times}10^{15}$ cm^{-2} and excitation temperatures of 150 (blue) and 300 K (red) are overplotted. The synthetic spectrum of the entire molecular inventory determined with PILS data towards this position is plotted in green. The quantum numbers of the transition are indicated at the top of each panel and the upper state energy is given in the top left of each panel.

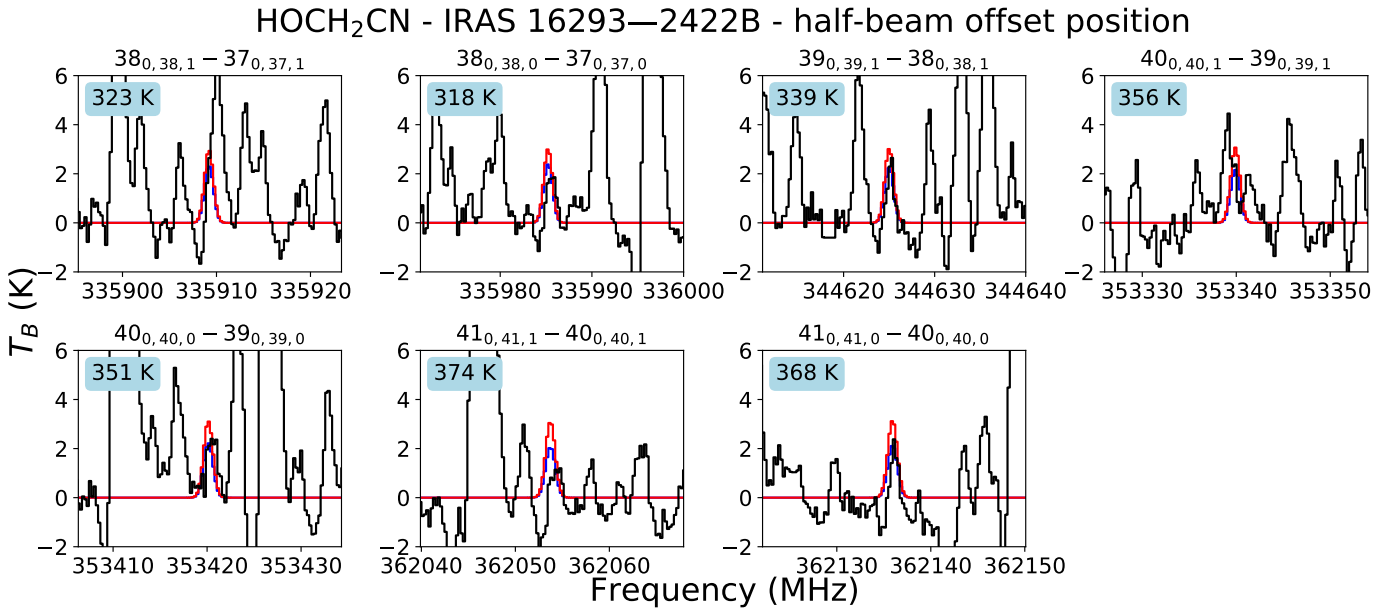


Fig. (7) Overview of a-type ($J'_{0,J'} - J''_{0,J''}$) $HOCH_2CN$ transitions covered by the PILS spectrum towards the half-beam offset position of IRAS 16293B, illustrating the detection of a number of these lines. The observed spectrum is plotted in black and synthetic spectra for a column density of $3.0{\times}10^{15}$ cm^{-2} and excitation temperatures of 150 (blue) and 300 K (red) are overplotted. The quantum numbers of the transition are indicated at the top of each panel and the upper state energy is given in the top left of each panel.

tion. CH_3NCO has been detected in multiple interstellar sources, but this is the first detection towards SMM1 and therefore also the first detection towards an intermediate-mass source. These new detections serve as additional evidence for a large and diverse reservoir of prebiotic molecules in star- and planet-forming regions, which can contribute to the emergence of biomolecules on planetary bodies. Of the C_2H_3NO isomers, CH_3NCO is energetically the most favorable, followed by $HOCH_2CN$, which has a higher relative energy of 12.1 – 18.6 kcal mol^{-1} (0.5 – 0.8 eV molecule^{-1} or 5800 – 9300 K molecule^{-1}), depending on the level of theory used (Fourré et al. 2020). In a thermodynamic equilibrium, lower energy or more stable products are favored and in such a scenario, CH_3NCO is expected to be more abundant than $HOCH_2CN$ by a factor of at least $1{\times}10^9$ (assuming a

temperature of 300 K). The fact that CH_3NCO and $HOCH_2CN$ are found to be equally abundant is, therefore, evidence that the formation of these molecules is rather driven by kinetics.

To better understand the interstellar chemistry of $HOCH_2CN$ and CH_3NCO, their abundances and those of several other species are compared for SMM1-a, IRAS 16293B, and several other sources for which at least some of these species are detected. For this comparison, it is important to emphasise observational differences. For example, SMM1 (D ≈436 pc) is located further away than IRAS 16293 (D ≈141 pc, Dzib et al. 2018) and the beam size used in this work (1″.2) is larger than that of the PILS survey (0″.5). Therefore, the chemical inventory of SMM1-a and the involved chemical processes are investigated on a much larger spatial scale of roughly 500 au, compared to about 70 au for IRAS 16293B. The SMM1-a observations can cover a larger range of physical environments (e.g. also the envelope or outflow), and potentially a larger temperature gradient. At the same time, the higher luminosity of SMM1 results in a larger area where hot core conditions are present, thus compensating for the lower spatial resolution. Furthermore, the SMM1-a spectrum is extracted towards the continuum peak, but for IRAS 16293B a full-beam offset position from the continuum peak is used. Therefore, when comparing molecular ratios between the two sources, they may not only be affected by different physical conditions but also due to the way the sources were observed. Observational parameters of SMM1-a, IRAS 16293B, and other sources used for comparisons are listed in Table D.1.

$HOCH_2CN$ is thus far only detected in two sources, SMM1-a and IRAS 16293B (Zeng et al. 2019), and therefore a chemical comparison is limited to these two objects. To use molecular ratios that are unbiased by observational parameters, only data of the chemical inventory of IRAS 16293B obtained with PILS survey data at the full-beam offset position is used for the source comparison. This means that the tentative column density of $HOCH_2CN$ in IRAS 16293B is used. Figure 8 shows the abundances of molecules detected in this work to CH_3OH and HNCO in SMM1-a and IRAS 16293B. For IRAS 16293B, the analysis performed in this work is combined with results from Jørgensen et al. (2016); Coutens et al. (2016); Ligterink et al. (2017); Coutens et al. (2018); Persson et al. (2018); Calcutt et al. (2018); Jørgensen et al. (2018). For both the [X]/[CH_3OH] and [X]/[HNCO] ratios, all the oxygen-bearing molecules, CH_3CN, and NH_2CN are found to be more abundant in IRAS 16293B than in SMM1-a. For [X]/[CH_3OH] its ratios are generally a factor of a few lower in SMM1-a, while for the [X]/[HNCO] ratios the difference is usually more than a factor of ten.

4.1. SMM1-a: A $HOCH_2CN$-rich source

While general trends are found in the [X]/[CH_3OH] and [X]/[HNCO] ratios displayed in Fig. 8, three molecules deviate from the general trend. The abundance of CH_3NCO is found to be approximately equal in both sources, while $HOCH_2CN$ and HNCO are more abundant in SMM1-a compared to IRAS 16293B. In particular, for $HOCH_2CN$ a large difference is seen in its ratios to CH_3OH, which can be more than an order of magnitude different between the two sources.

To gain further insight in how the chemical compositions of SMM1-a and IRAS 16293B differ, the statistical distance of molecular ratios are plotted in Fig. 9. The statistical distance indicates how significant the difference in a molecular ratio between SMM1-a and IRAS 16293B is (see Manigand et al. 2020, and Appendix E). Greater values indicate a greater difference in the molecular ratios between the two sources. A positive value indicates that the ratio of SMM1-a is greater than that of IRAS 16293B and vice versa. Fig. 9 highlights that $HOCH_2CN$ and HNCO are more abundant in SMM1-a (σ ranging from 3 – 6) and CH_3NCO is moderately more abundant in SMM1-a ($\sigma \geq 2$).

The statistical distance results have several implications. Since the abundances of both $HOCH_2CN$ and HNCO are enhanced in SMM1-a, this may indicate a relationship between these two species. For CH_3NCO a much less significant enhancement is seen, which can imply that both C_2H_3NO isomers form via different chemical reactions or under different physical conditions. However, it is important to stress that an abundance correlation does not always imply a formational link between species (Belloche et al. 2020).

The statistical distances of ratios involving CH_3CN, NH_2CN, a-(CH_2OH), and CH_3CH_2OH show that there is almost no variation in these molecules between SMM1-a and IRAS 16293B. This is interesting because some of these molecules can form in reactions involving radicals from which $HOCH_2CN$ also can be formed, such as CN, CH_2OH, and CH_2CN. This hints that either $HOCH_2CN$ is not formed from these radicals, is not linked to the reaction networks that form the four aforementioned species, or $HOCH_2CN$ forms from the same radicals, but under different physical conditions.

Finally, it is interesting to note that ratios of D_2CO and CH_3OCHO to NH_2CN, CH_3CH_2OH, and a-$(CH_2OH)_2$ seem to be a bit more abundant in SMM1-a than in IRAS 16293B. This is particularly significant for the case of D_2CO since H_2CO is involved in the Strecker-like formation of $HOCH_2CN$, see reaction 2. A higher abundance of H_2CO may indicate that the Strecker-like reaction can more efficiently take place. However, care needs to be taken with this interpretation, since the D_2CO spectral lines in the SMM1-a spectrum are blended and thus there is a large uncertainty on its column density. At the same time, the D/H ratio of H_2CO is not known in SMM1-a, which introduces another source of uncertainty. To investigate if there is a correlation between $HOCH_2CN$ and H_2CO, both species should be identified towards more sources and H_2CO should be observed through its minor ^{13}C and ^{18}O isotopes instead of the deuterated species. For now, however, the Strecker-like synthesis of $HOCH_2CN$ in the ISM can neither be confirmed nor ruled out.

4.2. Interstellar formation of CH_3NCO

Since its first detection in the ISM, the formation of CH_3NCO has been hypothesised to be linked to that of HNCO, see Eq. 1. To investigate the interstellar chemical relationship between these two species, their gas-phase ratios towards interstellar sources are plotted in Fig. 10. The result of the SMM1-a analysis is complemented by data from the low-mass protostar IRAS 16239B (Ligterink et al. 2017), the quiescent giant molecular cloud G+0.693 (Zeng et al. 2018), the high-mass star-forming region Orion KL (Cernicharo et al. 2016), the high-mass hot molecular core G10.47+0.03 (Gorai et al. 2020), and the galactic center source Sagittarius B2(N) (Sgr B2(N), Belloche et al. 2013; Cernicharo et al. 2016; Belloche et al. 2017). The majority of these sources is categorised as hot cores or corinos. In these sources, thermal desorption of molecules from ice mantles plays an important role to chemically enrich the gas surrounding the protostar, in particular around the desorption temperature of water ice (~100 K). The exception is the source G+0.693, which is a molecular cloud. Molecules observed in the gas of this cloud are assumed to be the result of gas-phase

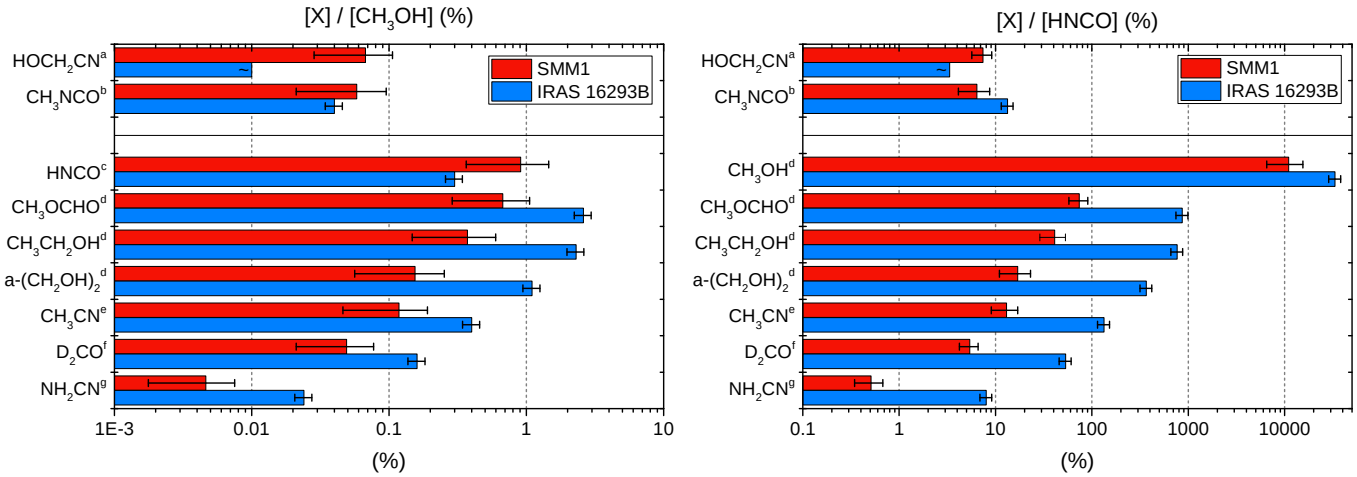


Fig. (8) Ratios of [X]/[CH_3OH] towards SMM1-a (red) and IRAS 16293B (blue) in decreasing order of SMM1-a abundance. The "~" symbol indicates that these $HOCH_2CN$ ratios have been determined with the column density of the tentative $HOCH_2CN$ detection towards the IRAS 16293B full-beam offset position. For IRAS 16293B, column densities derived towards the full-beam offset position from the following PILS publications are used: [a]This work, [b]Ligterink et al. (2017), [c]Coutens et al. (2016), [d]Jørgensen et al. (2016, 2018), [e]Calcutt et al. (2018), [f]Persson et al. (2018), [g]Coutens et al. (2018).

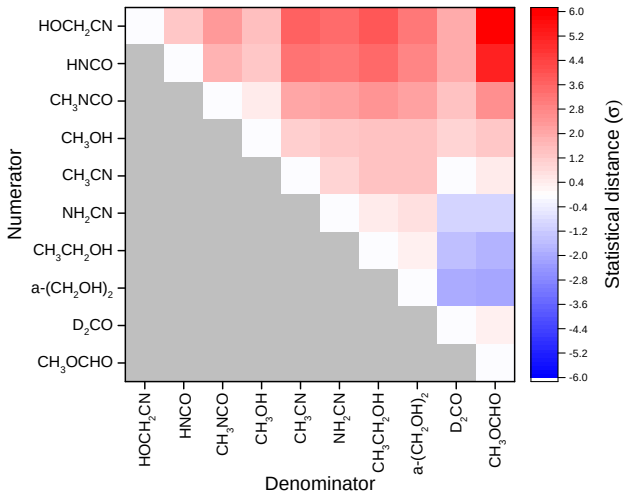


Fig. (9) Statistical distance between molecular ratios in SMM1 and IRAS 16293B, given in σ. Larger σ values indicate a larger difference between the two sources for a given ratio. Positive values indicate that a ratio is higher in SMM1-a, while negative values indicate that a ratio is lower in SMM1-a. In particular, all ratios of $HOCH_2CN$ are found to be higher in SMM1-a than in IRAS 16239B.

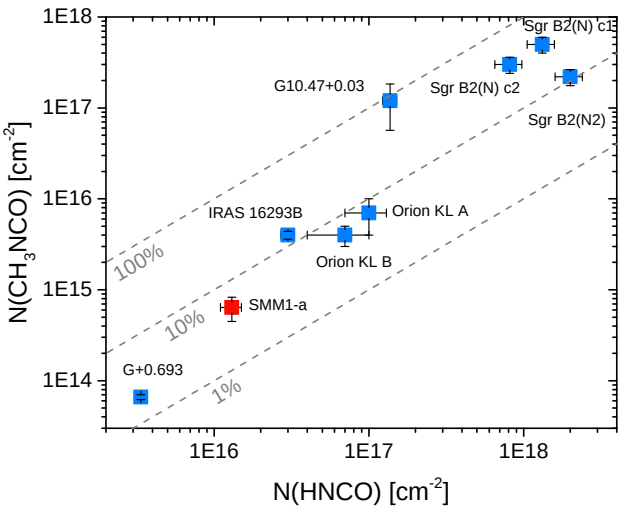


Fig. (10) Ratios of [CH_3NCO]/[HNCO] ratios towards SMM1-a and various other sources. Column densities from the following publications are used: Belloche et al. (2013), Cernicharo et al. (2016), Ligterink et al. (2017), Belloche et al. (2017), Zeng et al. (2018), Gorai et al. (2020), and this work.

formation reactions or non-thermal desorption from ice mantles of dust grains.

The ratios of CH_3NCO and HNCO are generally similar at [CH_3NCO] / [HNCO] = ~10% and vary only by a factor of a few, in particular when the lowest and highest ratio are omitted. The lowest ratio, found towards G+0.693, arises in a source with a very different physical structure and can therefore not directly be compared with the hot core and corino sources. The highest ratio is found towards G10.47+0.03, but the analysis of HNCO in this source is likely performed on optically thick HNCO lines and the analysis seems to underestimate the HNCO column density in this source (see Fig. 4 in Gorai et al. 2020). Removing these results from the analysis, a correlation between CH_3NCO and HNCO is found, which may indicate a chemical link between CH_3NCO and HNCO. Furthermore, this correlation spans a variety of sources of different masses and over four order of magnitude in luminosities. This results in different physical conditions, such as gas and dust temperature and radiation fields for each source. Therefore, the lack of source-to-source variation in [CH_3NCO]/[HNCO] ratio hints that the abundances of these species are set at an early stage of star formation. Formation of CH_3NCO via reaction 1 in the ice mantles of dust grains during the dark cloud stage or while the ice mantles are warmed up in the hot core/corino stage are a plausible scenario.

4.3. On the formation of -CN and -NCO molecules

Figure 9 shows that $HOCH_2CN$ and HNCO abundances are enhanced in SMM1-a compared to IRAS 16293B. At the same time, CH_3NCO is only marginally enhanced and CH_3CN and NH_2CN abundances show little difference between the two sources. Why the abundances of $HOCH_2CN$ and HNCO are enhanced in SMM1-a and those of CH_3NCO, CH_3CN, and NH_2CN are not is not straightforward to explain. However, it is likely that the various -CN and -NCO molecules form in different chemical reactions and physical conditions.

As this work shows, CH_3NCO probably forms at an early stage of star-formation, as do CH_3CN and NH_2CN. All three species are suggested to form in radical-radical addition reactions in ice mantles. These reactions take place during the dark cloud stage in cold (∼10 K) ice mantles and significantly speed up when the ice mantle temperature increases to ∼30 K and radicals become mobile (Garrod et al. 2008; Coutens et al. 2018). Some reactions can compete for the same radical, such as CH_3CN and NH_2CN, which both compete for the -CN radical.

The fact that $HOCH_2CN$ and HNCO are enhanced in abundance in SMM1-a, can indicate a link between these species. Both molecules can be formed from HCN in ice mantles of interstellar dust grains. $HOCH_2CN$ can be formed in the Strecker-like reaction when HCN is converted to CN^-. HNCO and the related anion OCN^- are formed when HCN:H_2O mixtures are processed with energetic UV photons or protons (Gerakines et al. 2004). These reactions are aided by high grain temperatures (≫30 K, but below the water sublimation temperature) for a prolonged time and high fluxes of photons and energetic particles. If these conditions are met in SMM1, they can explain the higher abundances of $HOCH_2CN$ and HNCO compared to IRAS 16239B and present a formational link between some -CN and -NCO molecules. However, only circumstantial evidence can be presented for such conditions in SMM1, which is based on the fact that SMM1 hosts multiple protostellar sources and outflows, which can warm and irradiate the cloud (e.g. Choi 2009; Dionatos et al. 2014; Hull et al. 2017; Tychoniec et al. 2019).

To gain further insight into the reactions that form -CN and -NCO molecules, unbiased observations of these species towards a multitude of sources spanning different physical conditions are needed. Not only the isomers $HOCH_2CN$ and CH_3NCO should be targeted for these observations, but also species like CH_3CN, HNCO, NH_2CN, C_2H_3CN, and C_2H_5CN. Laboratory, theoretical and modeling efforts should be focused on understanding the formation of these species. In particular, the formation of $HOCH_2CN$ via pathways other than the thermal Strecker-like synthesis needs to be studied and a better understanding of the formation of CH_3CN is required.

5. Conclusions

This publication presents the simultaneous detection of the C_2H_3NO isomers methyl isocyanate (CH_3NCO) and glycolonitrile ($HOCH_2CN$). Both species are identified towards the intermediate-mass Class 0 protostar Serpens SMM1-a. This is only the second interstellar detection of glycolonitrile, while for methyl isocyanate it is the first detection towards an intermediate-mass protostar. Additionally, CH_3OH, HNCO, CH_3OCHO, CH_3CH_2OH, a-$(CH_2OH)_2$, D_2CO, and NH_2CN are detected. CH_2CNH, CH(O)CN, and NH_2CH_2CN, molecules that are related to $HOCH_2CN$, are searched for but not identified. Data from the PILS survey towards IRAS 16293B are analysed in search for $HOCH_2CN$ and this molecule is identified in a spectrum extracted at a half-beam offset position from the continuum peak of IRAS 16239B. The molecules CH_2CNH, CH(O)CN, and NH_2CH_2CN are not identified towards this source.

The detection of CH_3NCO and $HOCH_2CN$ towards SMM1-a is additional evidence of a large interstellar reservoir of prebiotic molecules. Delivery of these molecules to planetary surfaces may contribute to the formation of biomolecules on these objects. The column densities and abundances of CH_3NCO (N_T = 6.4×10^{14} cm^{-2} and [CH_3NCO]/[CH_3OH] = 5.3×10^{-4}) and $HOCH_2CN$ (N_T = 7.4×10^{14} cm^{-2} and [$HOCH_2CN$]/[CH_3OH] = 6.2×10^{-4}) are found to be equal within their error bars. Since $HOCH_2CN$ is the least energetically favorable of the two isomers, thermodynamics predicts that CH_3NCO should be more abundant. The equal ratio between both molecules is therefore evidence that the formation of these molecules is driven by kinetics.

The comparison of molecular ratios between SMM1-a and IRAS 16293B show that $HOCH_2CN$ and HNCO are significantly more abundant in the former source. The molecular ratios of $HOCH_2CN$ hint that the formation of this molecule does not heavily depend on solid-state radical-radical addition reactions, such as $HOCH_2$ + CN and HO + CH_2CN. Formation via the thermal Strecker-like reaction [X^+CN^-] + H_2CO in ice mantles cannot be confirmed nor ruled out based on the current data but may be a prominent formation pathway.

To investigate the possibility that CH_3NCO formation is related to HNCO, the ratios of these molecules in SMM1-a and other sources are analysed. These ratios are found to be uniform throughout all sources at [CH_3NCO]/[HNCO] = ∼10 %. This indicates that there is a chemical link between both species, but also that its ratios is already set at an early stage of star-formation. Presumably CH_3NCO forms via the radical-radical reaction CH_3 + NCO in ice mantles during the dark cloud stage.

It is difficult to establish a chemical link between -CN and -NCO molecules. Some may be related, such as $HOCH_2CN$ and HNCO, which can both form from HCN at elevated (≫30 K) grain temperatures and in relatively high radiation fields. Continued observational, laboratory, and theoretical studies of -CN and -NCO molecules are required to gain further insight into their formation and links in their chemistry.

Acknowledgements. We thank E.G. Bøgelund, S.F. Wampfler, M.N. Drozdovskaya, B. Kulterer, and B.A. McGuire for helpful discussions on the observations, spectroscopy, and the chemistry of the C_2H_3NO isomers. The authors acknowledge assistance from Allegro, the European ALMA Regional Center node in the Netherlands. We thank the anonymous referee for their thorough review of this manuscript and helpful comments. This paper makes use of the following ALMA data: ADS/JAO.ALMA#2018.1.00836.S and ADS/JAO.ALMA#2013.1.00278.S. ALMA is a partnership of ESO (representing its member states), NSF (USA) and NINS (Japan), together with NRC (Canada), MOST and ASIAA (Taiwan), and KASI (Republic of Korea), in cooperation with the Republic of Chile. The Joint ALMA Observatory is operated by ESO, AUI/NRAO and NAOJ. NFWL is supported by the Swiss National Science Foundation (SNSF) Ambizione grant 193453. JKJ is supported by the European Research Council (ERC) under the European Union's Horizon 2020 research and innovation programme through ERC Consolidator Grant "S4F" (grant agreement No 646908). AC acknowledges financial support from the Agence Nationale de la Recherche (grant ANR-19-ERC7-0001-01).

References

Allamandola, L., Sandford, S., & Valero, G. 1988, Icarus, 76, 225
Belloche, A., Garrod, R. T., Müller, H. S. P., et al. 2019, A&A, 628, A10
Belloche, A., Maury, A., Maret, S., et al. 2020, Astronomy & Astrophysics
Belloche, A., Menten, K., Comito, C., et al. 2008, Astronomy & Astrophysics, 482, 179
Belloche, A., Meshcheryakov, A. A., Garrod, R. T., et al. 2017, A&A, 601, A49

Belloche, A., Müller, H. S., Menten, K. M., Schilke, P., & Comito, C. 2013, Astronomy & Astrophysics, 559, A47
Bocquet, R., Demaison, J., Cosléou, J., et al. 1999, Journal of molecular spectroscopy, 195, 345
Bøgelund, E. G., McGuire, B. A., Hogerheijde, M. R., van Dishoeck, E. F., & Ligterink, N. F. W. 2019, A&A, 624, A82
Boogert, A. A., Gerakines, P. A., & Whittet, D. C. 2015, Annual Review of Astronomy and Astrophysics, 53
Bossa, J., Theule, P., Duvernay, F., & Chiavassa, T. 2009, The Astrophysical Journal, 707, 1524
Bulak, M., Paardekooper, D., Fedoseev, G., & Linnartz, H. 2020, Astronomy & Astrophysics, 636, A32
Calcutt, H., Jørgensen, J. K., Müller, H., et al. 2018, Astronomy & Astrophysics, 616, A90
Casali, M., Eiroa, C., & Duncan, W. 1993, Astronomy and Astrophysics, 275, 195
Cernicharo, J., Kisiel, Z., Tercero, B., et al. 2016, Astronomy & Astrophysics, 587, L4
Choi, M. 2009, The Astrophysical Journal, 705, 1730
Christen, D., Coudert, L., Suenram, R. D., & Lovas, F. J. 1995, Journal of Molecular Spectroscopy, 172, 57
Christen, D. & Müller, H. S. 2003, Physical Chemistry Chemical Physics, 5, 3600
Coutens, A., Jørgensen, J. K., Van der Wiel, M. H. D., et al. 2016, Astronomy & Astrophysics, 590, L6
Coutens, A., Ligterink, N. F. W., Loison, J.-C., et al. 2019, Astronomy & Astrophysics, 623, L13
Coutens, A., Willis, E., Garrod, R., et al. 2018, Astronomy & Astrophysics, 612, A107
Danger, G., Borget, F., Chomat, M., et al. 2011, Astronomy & Astrophysics, 535, A47
Danger, G., Duvernay, F., Theulé, P., Borget, F., & Chiavassa, T. 2012, The Astrophysical Journal, 756, 11
Danger, G., Rimola, A., Mrad, N. A., et al. 2014, Physical Chemistry Chemical Physics, 16, 3360
Dionatos, O., Jørgensen, J. K., Green, J. D., et al. 2013, Astronomy & Astrophysics, 558, A88
Dionatos, O., Jørgensen, J. K., Teixeira, P., Güdel, M., & Bergin, E. 2014, Astronomy & Astrophysics, 563, A28
Dzib, S., Ortiz-León, G., Hernández-Gómez, A., et al. 2018, Astronomy & Astrophysics, 614, A20
Fisher, J., Paciga, G., Xu, L.-H., et al. 2007, Journal of Molecular Spectroscopy, 245, 7
Fourré, I., Matz, O., Ellinger, Y., & Guillemin, J. 2020, Astronomy & Astrophysics, 639, A16
Garrod, R. T., Weaver, S. L. W., & Herbst, E. 2008, The Astrophysical Journal, 682, 283
Gerakines, P., Moore, M., & Hudson, R. 2004, Icarus, 170, 202
Goicoechea, J. R., Cernicharo, J., Karska, A., et al. 2012, Astronomy & Astrophysics, 548, A77
Gorai, P., Bhat, B., Sil, M., et al. 2020, The Astrophysical Journal, 895, 86
Halfen, D., Ilyushin, V. V., & Ziurys, L. M. 2015, The Astrophysical Journal Letters, 812, L5
Halfen, D. T., Ilyushin, V., & Ziurys, L. M. 2011, ApJ, 743, 60
Hocking, W., Gerry, M., & Winnewisser, G. 1975, Canadian Journal of Physics, 53, 1869
Högbom, J. A. 1974, A&AS, 15, 417
Hogerheijde, M. R., Van Dishoeck, E. F., Salverda, J. M., & Blake, G. A. 1999, The Astrophysical Journal, 513, 350
Hollis, J. M., Lovas, F. J., & Jewell, P. R. 2000, The Astrophysical Journal Letters, 540, L107
Hollis, J. M., Lovas, F. J., Remijan, A. J., et al. 2006, ApJ, 643, L25
Holtom, P. D., Bennett, C. J., Osamura, Y., Mason, N. J., & Kaiser, R. I. 2005, ApJ, 626, 940
Hudson, R. & Moore, M. 2004, Icarus, 172, 466
Hull, C. L., Girart, J. M., Kristensen, L. E., et al. 2016, The Astrophysical Journal Letters, 823, L27
Hull, C. L., Girart, J. M., Tychoniec, Ł., et al. 2017, The Astrophysical Journal, 847, 92
Ilyushin, V., Kryvda, A., & Alekseev, E. 2009, Journal of Molecular Spectroscopy, 255, 32
Jacobsen, S., Jørgensen, J., Van der Wiel, M., et al. 2018, Astronomy & Astrophysics, 612, A72
Jørgensen, J., Müller, H., Calcutt, H., et al. 2018, Astronomy & Astrophysics, 620, A170
Jørgensen, J. K., Favre, C., Bisschop, S. E., et al. 2012, The Astrophysical Journal Letters, 757, L4
Jørgensen, J. K., Van der Wiel, M. H. D., Coutens, A., et al. 2016, Astronomy & Astrophysics, 595, A117
Kaifu, N., Morimoto, M., Nagane, K., et al. 1974, ApJ, 191, L135
Koivusaari, M., Horneman, V., & Anttila, R. 1992, Journal of Molecular Spectroscopy, 152, 377
Kristensen, L., Van Dishoeck, E., Van Kempen, T., et al. 2010, Astronomy & Astrophysics, 516, A57
Kukolich, S. G., Nelson, A., & Yamanashi, B. 1971, Journal of the American Chemical Society, 93, 6769
Lapinov, A., Golubiatnikov, G. Y., Markov, V., & Guarnieri, A. 2007, Astronomy Letters, 33, 121
Lee, C.-W., Kim, J.-K., Moon, E.-S., Minh, Y. C., & Kang, H. 2009, ApJ, 697, 428
Ligterink, N., Coutens, A., Kofman, V., et al. 2017, Monthly Notices of the Royal Astronomical Society, 469, 2219
Ligterink, N. F., El-Abd, S. J., Brogan, C. L., et al. 2020, The Astrophysical Journal, 901, 37
Ligterink, N. F. W., Calcutt, H., Coutens, A., et al. 2018, Astronomy & Astrophysics, 619, A28
Majumdar, L., Loison, J.-C., Ruaud, M., et al. 2018, Monthly Notices of the Royal Astronomical Society: Letters, 473, L59
Manigand, S., Jørgensen, J., Calcutt, H., et al. 2020, Astronomy & Astrophysics, 635, A48
Margulès, L., McGuire, B., Senent, M. L., et al. 2017, Astronomy & Astrophysics, 601, A50
Martín-Doménech, R., Rivilla, V., Jiménez-Serra, I., et al. 2017, Monthly Notices of the Royal Astronomical Society, 469, 2230
Maté, B., Molpeceres, G., Tanarro, I., et al. 2018, The Astrophysical Journal, 861, 61
McGuire, B. A., Carroll, P. B., Loomis, R. A., et al. 2016, Science, 352, 1449
Müller, H. S., Belloche, A., Xu, L.-H., et al. 2016, Astronomy & Astrophysics, 587, A92
Müller, H. S., Brown, L. R., Drouin, B. J., et al. 2015, Journal of Molecular Spectroscopy, 312, 22
Müller, H. S., Schlöder, F., Stutzki, J., & Winnewisser, G. 2005, Journal of Molecular Structure, 742, 215
Müller, H. S., Thorwirth, S., Roth, D., & Winnewisser, G. 2001, Astronomy & Astrophysics, 370, L49
Niedenhoff, M., Yamada, K., Belov, S., & Winnewisser, G. 1995, Journal of Molecular Spectroscopy, 174, 151
Öberg, K. I., Van der Marel, N., Kristensen, L. E., & Van Dishoeck, E. F. 2011, The Astrophysical Journal, 740, 14
Ortiz-León, G. N., Dzib, S. A., Kounkel, M. A., et al. 2017, The Astrophysical Journal, 834, 143
Pearson, J. C., Brauer, C. S., & Drouin, B. J. 2008, Journal of Molecular Spectroscopy, 251, 394
Persson, M. V., Jørgensen, J. K., Müller, H., et al. 2018, Astronomy & Astrophysics, 610, A54
Pickett, H., Poynter, R., Cohen, E., et al. 1998, Journal of Quantitative Spectroscopy and Radiative Transfer, 60, 883
Quénard, D., Jiménez-Serra, I., Viti, S., Holdship, J., & Coutens, A. 2018, Monthly Notices of the Royal Astronomical Society, 474, 2796
Read, W. G., Cohen, E. A., & Pickett, H. M. 1986, Journal of Molecular Spectroscopy, 115, 316
Rivilla, V., Martín-Pintado, J., Jiménez-Serra, I., et al. 2019, Monthly Notices of the Royal Astronomical Society: Letters, 483, L114
Rivilla, V. M., Martín-Pintado, J., Jiménez-Serra, I., et al. 2020, The Astrophysical Journal Letters, 899, L28
Rubin, R. H., Swenson, G. W., J., Benson, R. C., Tigelaar, H. L., & Flygare, W. H. 1971, ApJ, 169, L39
Saladino, R., Crestini, C., Pino, S., Costanzo, G., & Di Mauro, E. 2012, Physics of Life Reviews, 9, 84
Sánchez-Monge, Á., Schilke, P., Ginsburg, A., Cesaroni, R., & Schmiedeke, A. 2018, Astronomy & Astrophysics, 609, A101
Sandford, S. A., Nuevo, M., Bera, P. P., & Lee, T. J. 2020, Chemical Reviews
Schwartz, A. W. & Goverde, M. 1982, Journal of molecular evolution, 18, 351
Schwartz, A. W., Joosten, H., & Voet, A. 1982, Biosystems, 15, 191
Turner, B. E., Liszt, H. S., Kaifu, N., & Kisliakov, A. G. 1975, ApJ, 201, L149
Tychoniec, Ł., Hull, C. L. H., Kristensen, L. E., et al. 2019, A&A, 632, A101
White, G. J., Casali, M. M., & Eiroa, C. 1995, Astronomy & Astrophysics, 298, 594
Wilson, T. 1999, Reports on Progress in Physics, 62, 143
Woon, D. E. 2001, Icarus, 149, 277
Xu, L.-H., Fisher, J., Lees, R., et al. 2008, Journal of Molecular Spectroscopy, 251, 305
Yan, Y., Zhang, J., Henkel, C., et al. 2019, The Astrophysical Journal, 877, 154
Zakharenko, O., Motiyenko, R. A., Margulès, L., & Huet, T. R. 2015, Journal of Molecular Spectroscopy, 317, 41
Zaleski, D. P., Seifert, N. A., Steber, A. L., et al. 2013, The Astrophysical Journal Letters, 765, L10
Zeng, S., Jiménez-Serra, I., Rivilla, V., et al. 2018, Monthly Notices of the Royal Astronomical Society, 478, 2962
Zeng, S., Quénard, D., Jiménez-Serra, I., et al. 2019, Monthly Notices of the Royal Astronomical Society: Letters, 484, L43

Appendix A: Spectroscopic data

In this paper, the CDMS and JPL spectroscopic databases are the primary sources of molecular line lists. In the following table, an overview of the analysed molecules, their identifier and catalog, and the most important publications in literature on which these entries are based is given.

Appendix B: Supporting information for the SMM1-a analysis

Appendix C: Analysis of PILS data

Appendix D: Source parameters

Appendix E: Statistical distance

The statistical distance of molecular ratios between SMM1-a and IRAS 16293B is calculated according to the following equation:

$$S_{\mathrm{X/Y}} = \frac{\left(\frac{N_{\mathrm{X}}}{N_{\mathrm{Y}}}\right)_{\mathrm{SMM1-a}} - \left(\frac{N_{\mathrm{X}}}{N_{\mathrm{Y}}}\right)_{\mathrm{IRAS\ 16293B}}}{\sqrt{\sigma^2_{\mathrm{SMM1-a}} + \sigma^2_{\mathrm{IRAS\ 16293B}}}}, \tag{E.1}$$

where N_{x} and N_{y} are the column densities of two different molecules and σ is the uncertainty on the column density ratio $\left(\frac{N_{\mathrm{X}}}{N_{\mathrm{Y}}}\right)$. The value of $S_{\mathrm{X/Y}}$ is given in σ and indicates the significance of the difference, with greater values implying that there is a more significant difference between the two sources. In this equation, positive values indicate that $\left(\frac{N_{\mathrm{X}}}{N_{\mathrm{Y}}}\right)$ is more abundant in SMM1-a than in IRAS 16293B, while negative values indicate the opposite.

Table (A.1)

Molecule	ID	catalog	entry date	reference
D_2CO	32502	CDMS	Jan 2016	Bocquet et al. (1999)
				Zakharenko et al. (2015)
$^{12}CH_3OH$	32504	CDMS	May 2016	Xu et al. (2008)
$CH_3^{18}OH$	34504	CDMS	Sep 2020	Fisher et al. (2007)
CH_3CN, ν_8=1	41509	CDMS	Nov 2016	Müller et al. (2015)
				Koivusaari et al. (1992)
NH_2CN	42003	JPL	Jan 1991	Read et al. (1986)
$HN^{12}CO$	43511	CDMS	May 2009	Kukolich et al. (1971)
				Hocking et al. (1975)
				Niedenhoff et al. (1995)
				Lapinov et al. (2007)
$HN^{13}CO$	44008	JPL	Jul 1987	Hocking et al. (1975)
CH_3CH_2OH	46524	CDMS	Nov 2016	Pearson et al. (2008)
				Müller et al. (2016)
CH_3NCO, ν=0	57505	CDMS	Mar 2016	Cernicharo et al. (2016)
CH_3NCO, ν=1	57506	CDMS	Mar 2016	Cernicharo et al. (2016)
$HOCH_2CN$	57512	CDMS	Mar 2017	Margulès et al. (2017)
CH_3OCHO	60003	JPL	Apr 2009	Ilyushin et al. (2009)
a-$(CH_2OH)_2$	62503	CDMS	Sep 2003	Christen et al. (1995)
				Christen & Müller (2003)

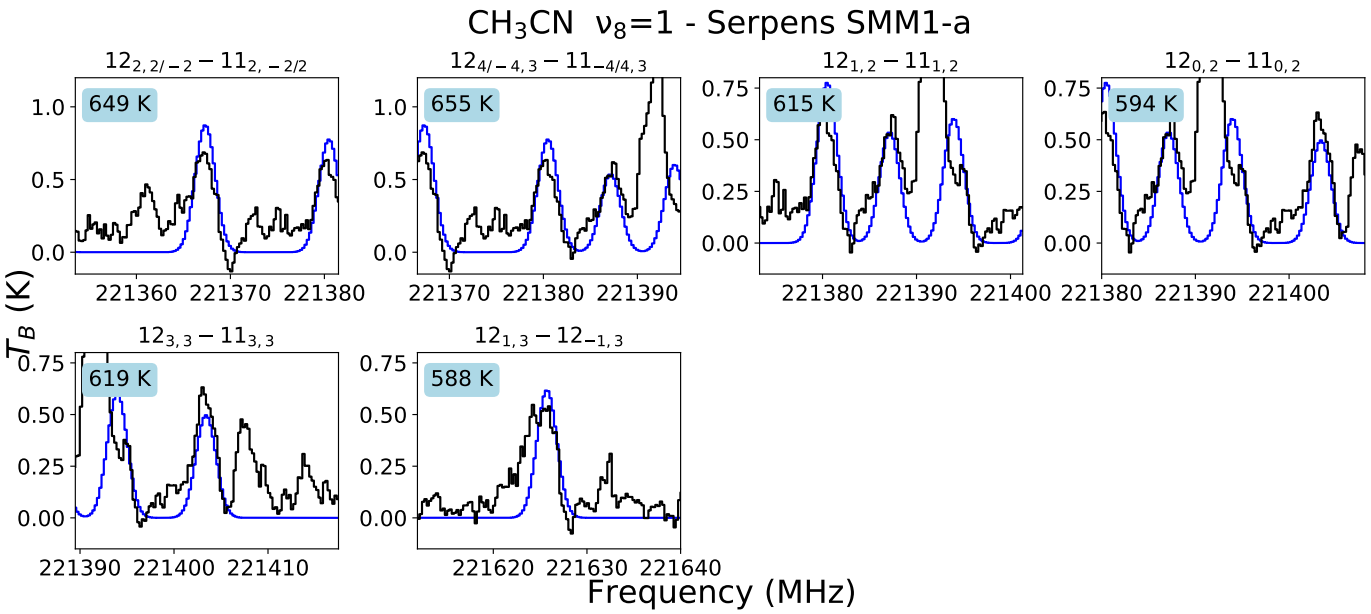


Fig. (B.1) Identified lines of CH_3CN ν_8=1 towards SMM1. The observed spectrum is plotted in black, with the best-fit synthetic spectrum overplotted in blue (N_T = (1.3±0.3)×10^{15} cm^{-2}, T_{ex} = 190±25 K). The transition is indicated at the top of each panel and the upper state energy is given in the top left of each panel.

Table (D.1) Physical parameters of interstellar sources used for abundance comparison.

Source	Telescope	Distance (pc)	Luminosity $L_\odot$	Beam size ($'' \times ''$)	physical size au	Reference
IRAS 16293–2422B	ALMA	141	3^a	0.5×0.5	70	Jørgensen et al. (2016)
Serpens SMM1-a	ALMA	436	100^b	1.3×1.0	500	this work
Orion KL	ALMA	414	1×10^5	1.8×1.8	750	Cernicharo et al. (2016)
Sgr B2(N2)	ALMA	8300	4.7×10^6	1.6×1.2 – 2.9×1.5	1.3×10^4	Belloche et al. (2017)
G10.47+0.03	ALMA	8550	5×10^5	2.0×1.4 – 2.4×1.6	1.6×10^4	Gorai et al. (2020)
Sgr B2(N)	IRAM 30m	8300	4.7×10^6	3.2×2.8 – 12.2×4.4	3.0×10^4	Cernicharo et al. (2016)
G+0.693	IRAM 30m & GBT	8300^c	–	9×9 – 55×55	≥7.5×10^4	Zeng et al. (2019)

Notes. [a]Luminosity determined from a modeling investigation by Jacobsen et al. (2018). [b]Luminosity for the entire SMM1 source. [c]The distance to G+0.693 is assumed to be the same as Sgr B2.

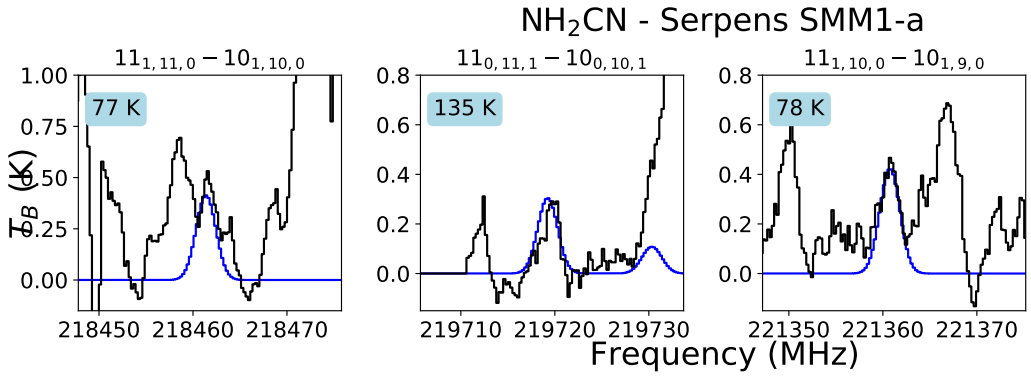


Fig. (B.2) Identified lines of NH_2CN towards SMM1. The observed spectrum is plotted in black, with the best-fit synthetic spectrum overplotted in blue (N_T = (5.1±1.3)×10^{13} cm^{-2}, T_{ex} = 190±40 K). The transition is indicated at the top of each panel and the upper state energy is given in the top left of each panel.

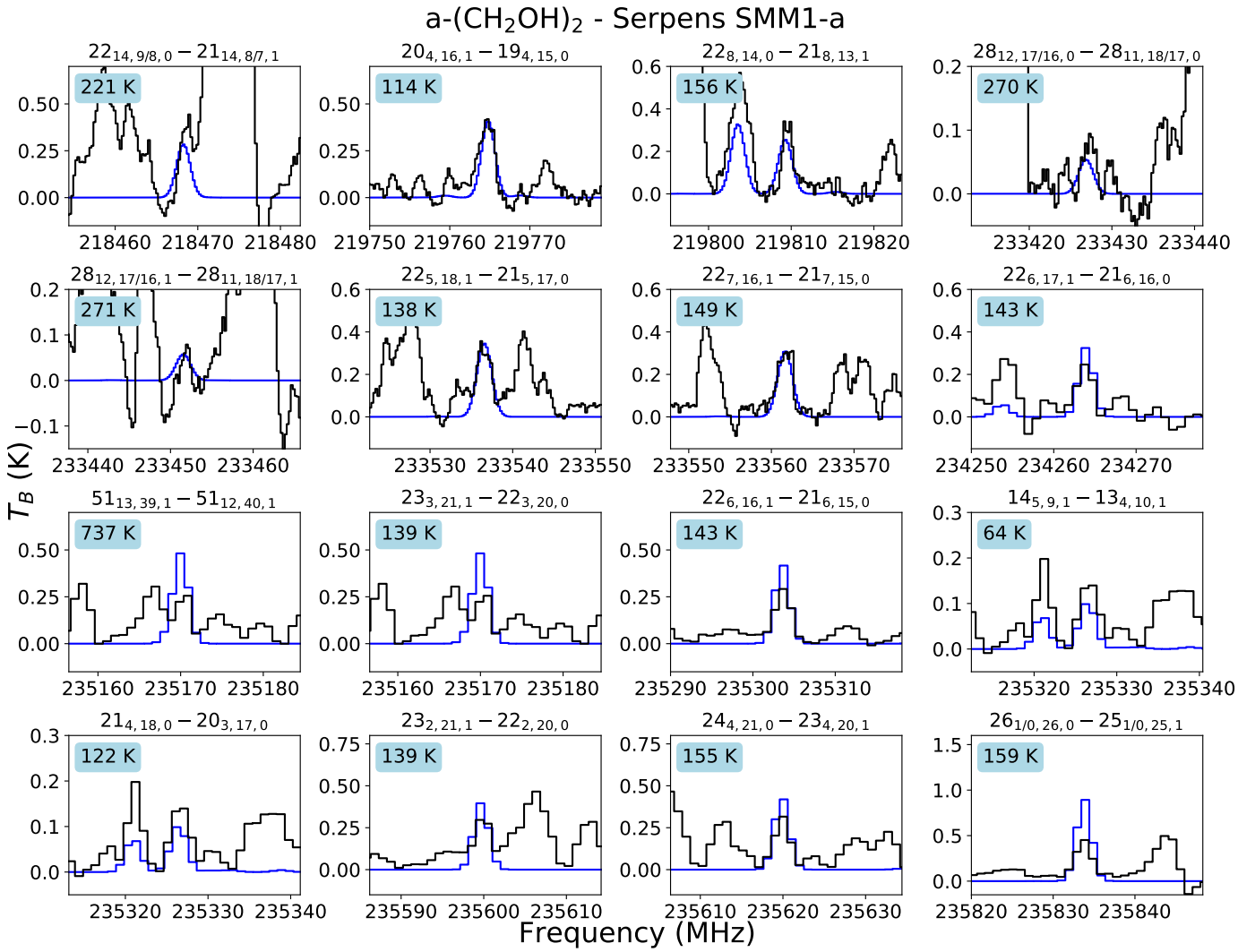


Fig. (B.3) Identified lines of a-$(CH_2OH)_2$ towards SMM1. The observed spectrum is plotted in black, with the best-fit synthetic spectrum overplotted in blue (N_T = (1.7±0.5)×10^{15} cm^{-2}, T_{ex} = 195±70 K). The transition is indicated at the top of each panel and the upper state energy is given in the top left of each panel.

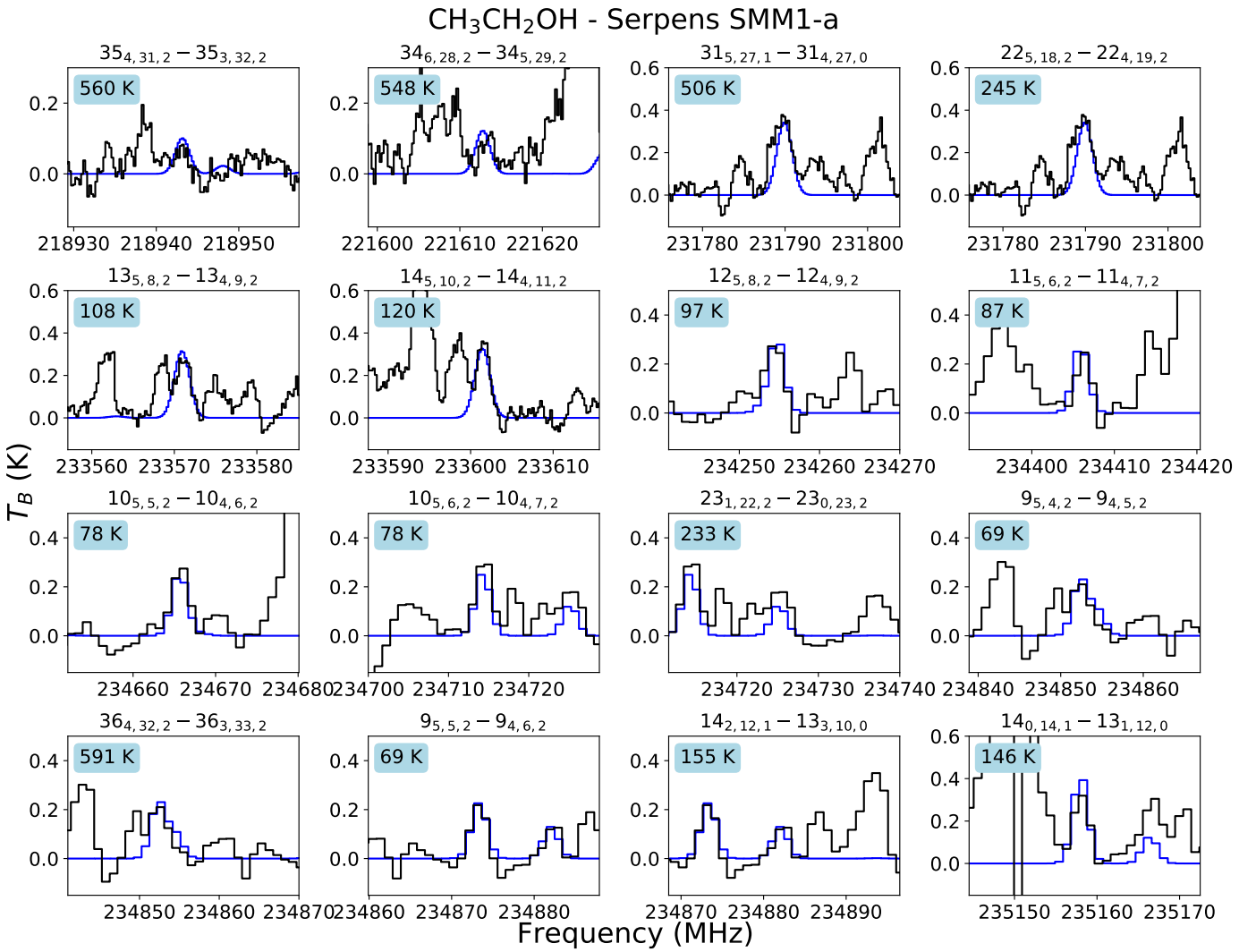


Fig. (B.4) Identified lines of CH_3CH_2OH towards SMM1. The observed spectrum is plotted in black, with the best-fit synthetic spectrum overplotted in blue (N_T = (4.1±0.9)×10^{15} cm^{-2}, T_{ex} = 210±25 K). The transition is indicated at the top of each panel and the upper state energy is given in the top left of each panel.

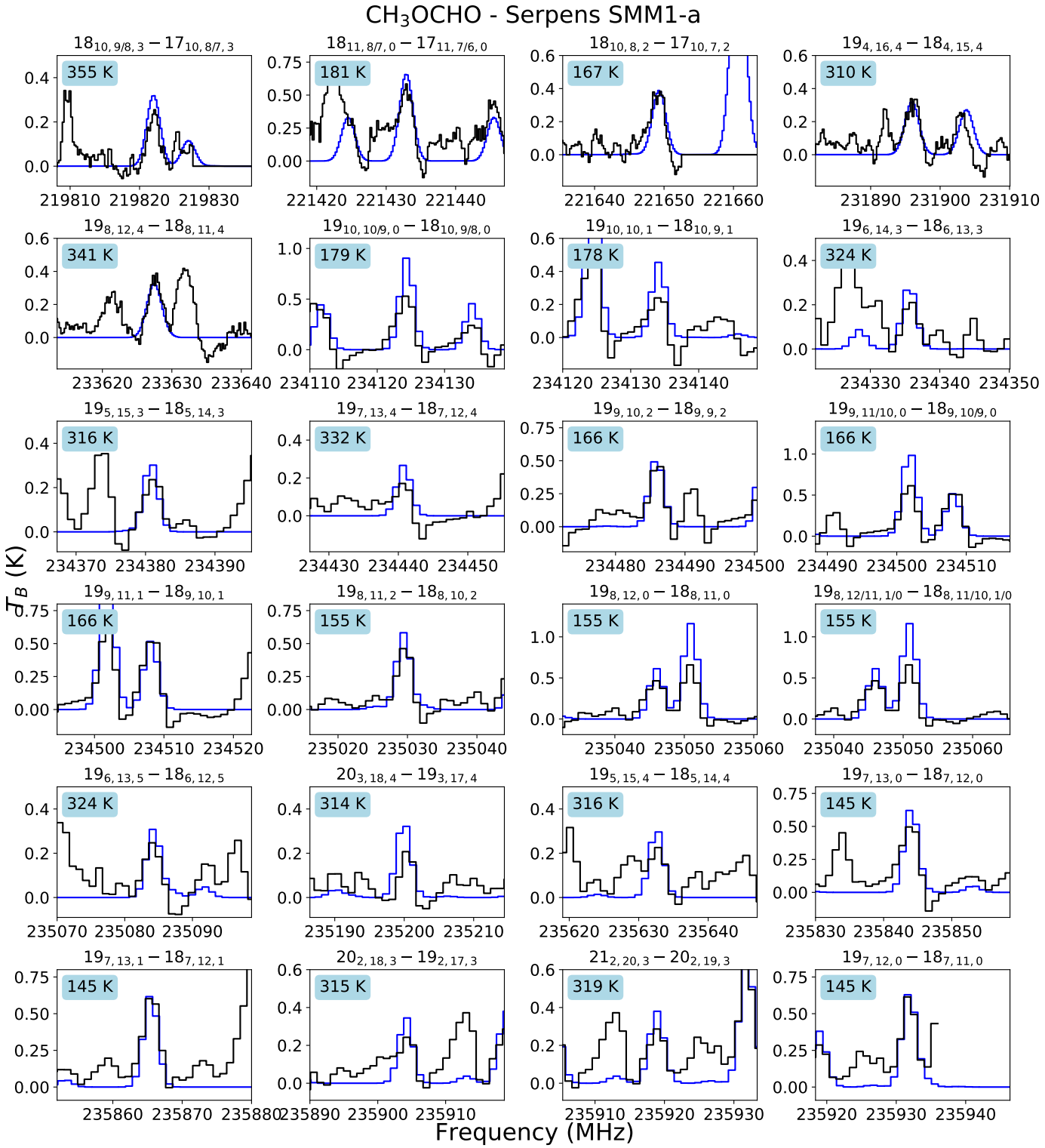


Fig. (B.5) Identified lines of CH_3OCHO towards SMM1. The observed spectrum is plotted in black, with the best-fit synthetic spectrum overplotted in blue (N_T = (7.4±0.7)×10^{15} cm^{-2}, T_{ex} = 215±20 K). The transition is indicated at the top of each panel and the upper state energy is given in the top left of each panel.

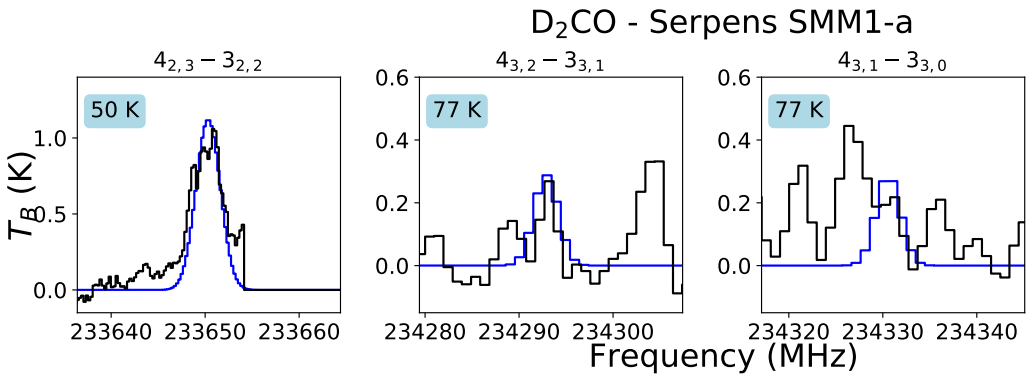


Fig. (B.6) Identified lines of D_2CO towards SMM1. The observed spectrum is plotted in black, with the best-fit synthetic spectrum overplotted in blue (N_T = (5.4±0.5)×10^{14} cm^{-2}, T_{ex} = [200] K). The transition is indicated at the top of each panel and the upper state energy is given in the top left of each panel.

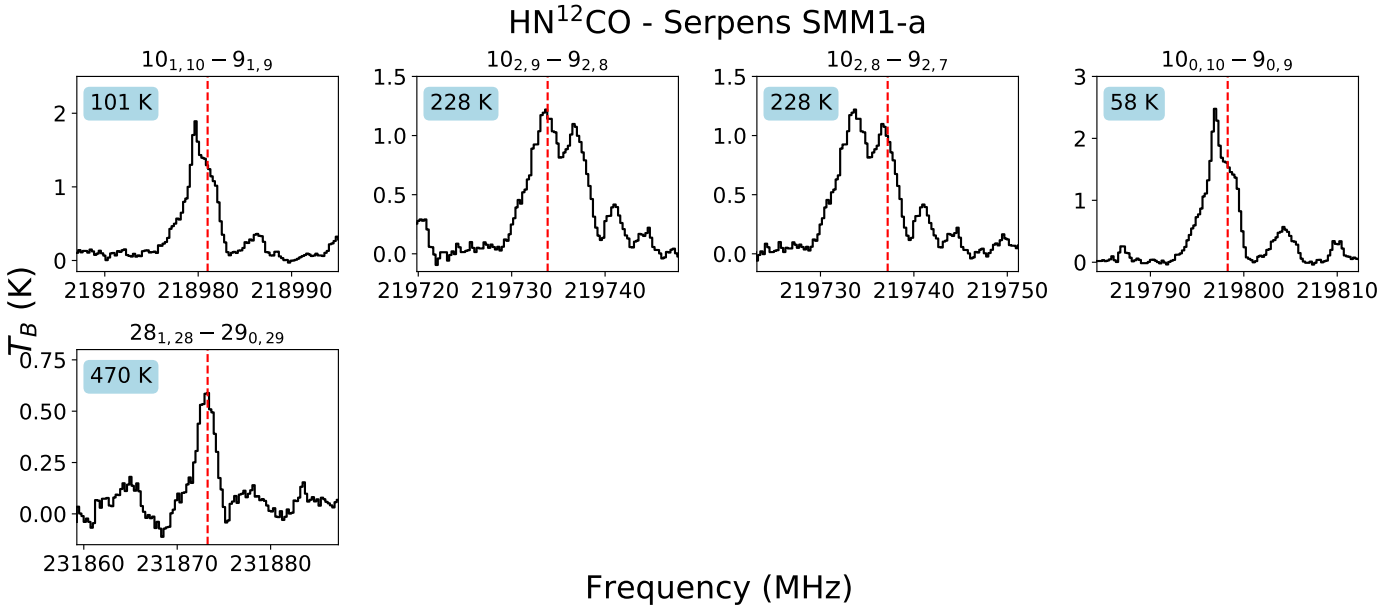


Fig. (B.7) Identified lines of $HN^{12}CO$ towards SMM1. The observed spectrum is plotted in black and the line position is indicated by the red dotted line. Because these lines are optically thick, not synthetic fit is given. The transition is indicated at the top of each panel and the upper state energy is given in the top left of each panel.

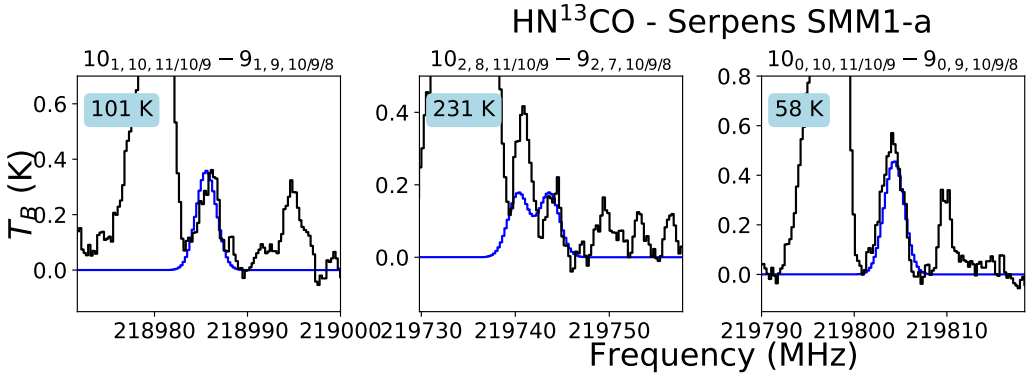


Fig. (B.8) Identified lines of $HN^{13}CO$ towards SMM1. The observed spectrum is plotted in black, with the best-fit synthetic spectrum overplotted in blue (N_T = (1.9±0.3)×10^{14} cm^{-2}, T_{ex} = 190±30 K). The transition is indicated at the top of each panel and the upper state energy is given in the top left of each panel.

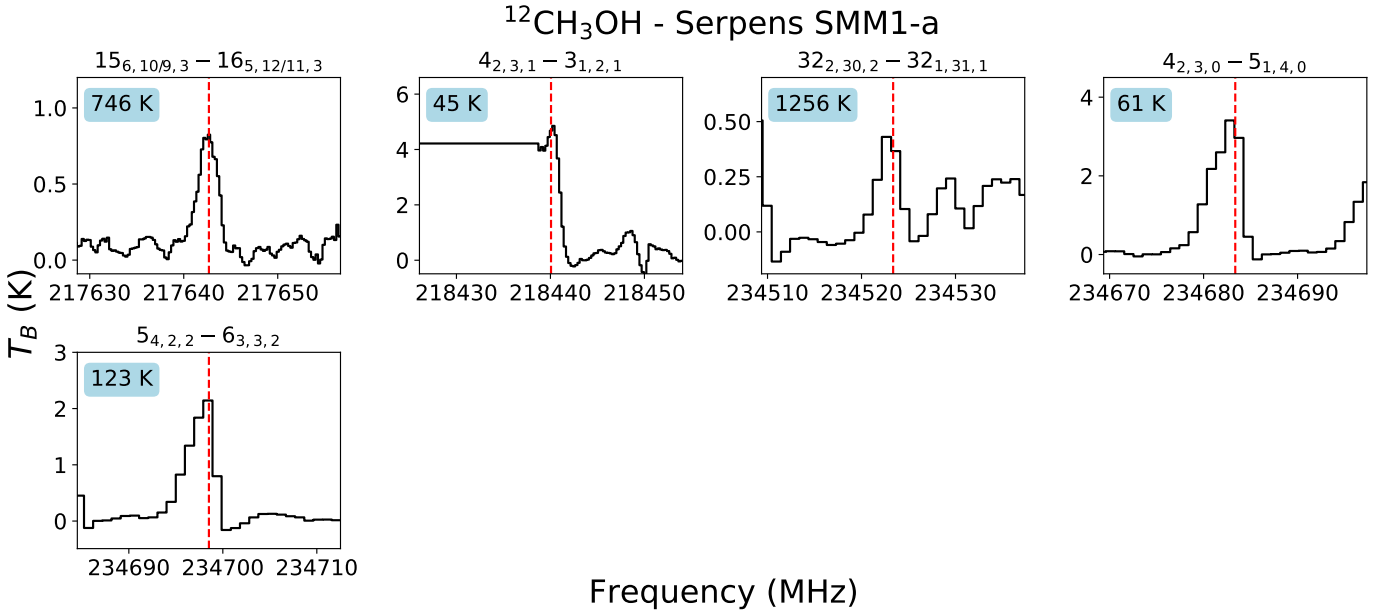


Fig. (B.9) Identified lines of $^{12}CH_3OH$ towards SMM1. The observed spectrum is plotted in black and the line position is indicated by the red dotted line. Because these lines are optically thick, not synthetic fit is given. The transition is indicated at the top of each panel and the upper state energy is given in the top left of each panel.

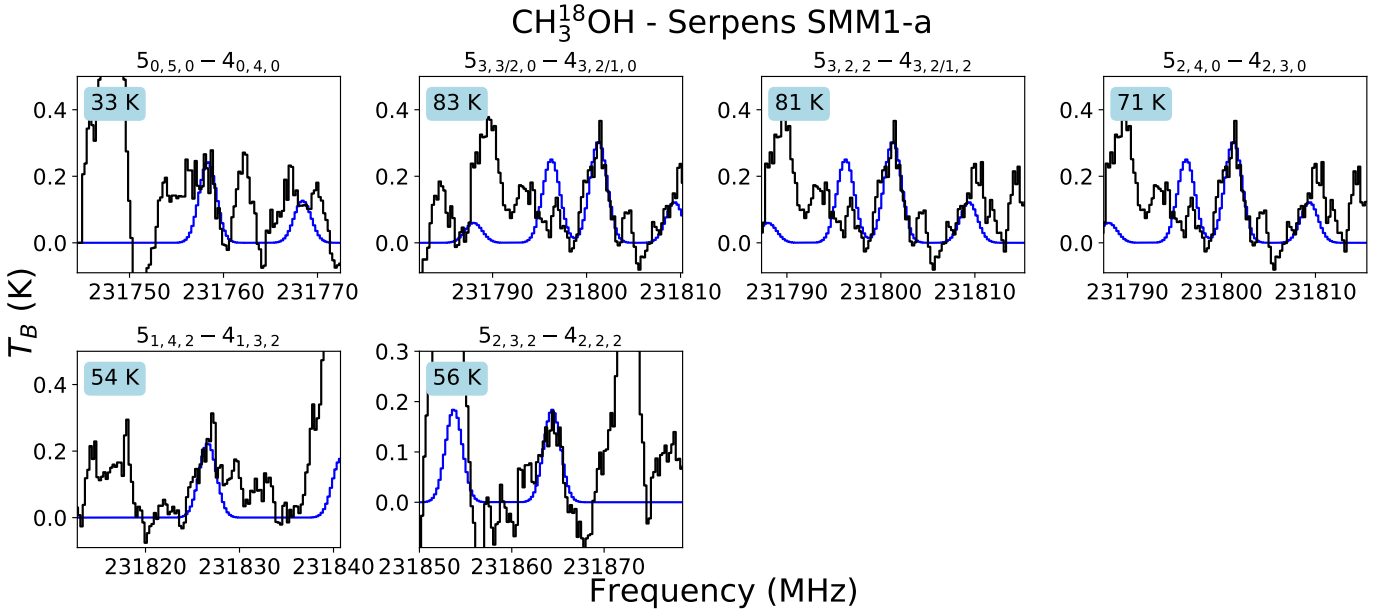


Fig. (B.10) Identified lines of $CH_3^{18}OH$ towards SMM1. The observed spectrum is plotted in black, with the best-fit synthetic spectrum overplotted in blue (N_T = (2.0±0.7)×10^{15} cm^{-2}, T_{ex} = 250±60 K). The transition is indicated at the top of each panel and the upper state energy is given in the top left of each panel.

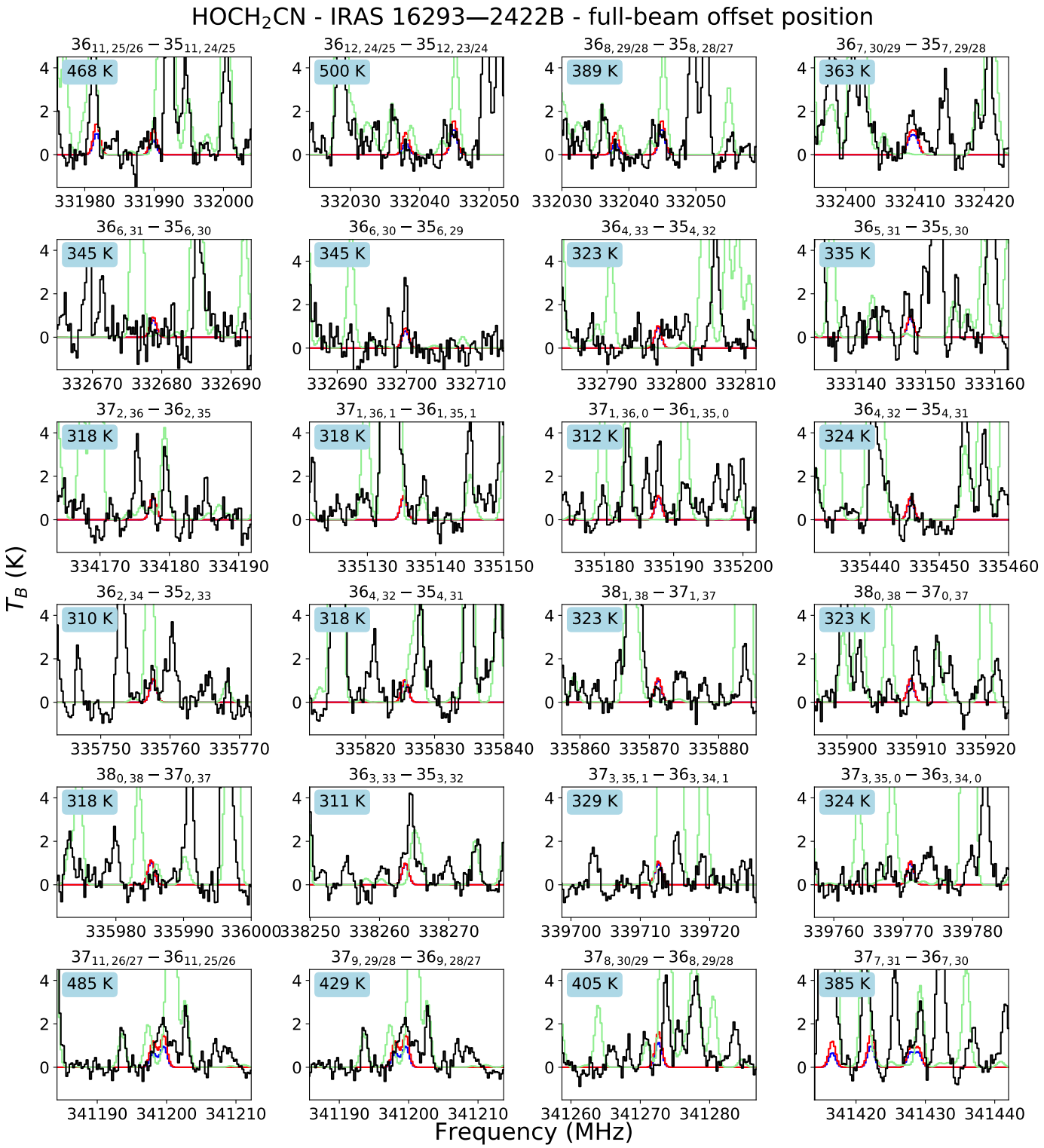


Fig. (C.1) Spectral lines of $HOCH_2CN$ in the PILS spectrum towards IRAS 16293B at the full-beam offset position. The observed spectrum is plotted in black, with synthetic spectra overplotted (N_T = [1.0×10^{15}] cm^{-2}, T_{ex} = 150, blue, and 300 K, red). The synthetic spectrum of the entire molecular inventory determined with PILS data towards this position is plotted in green. All covered transitions with $A_{ij} \geq 1.0\times10^{-3}$ s^{-1} that are not blended are shown. The transition is indicated at the top of each panel and the upper state energy is given in the top left of each panel. $HOCH_2CN$ is not detected in the full-beam offset position spectrum towards IRAS 16293B.

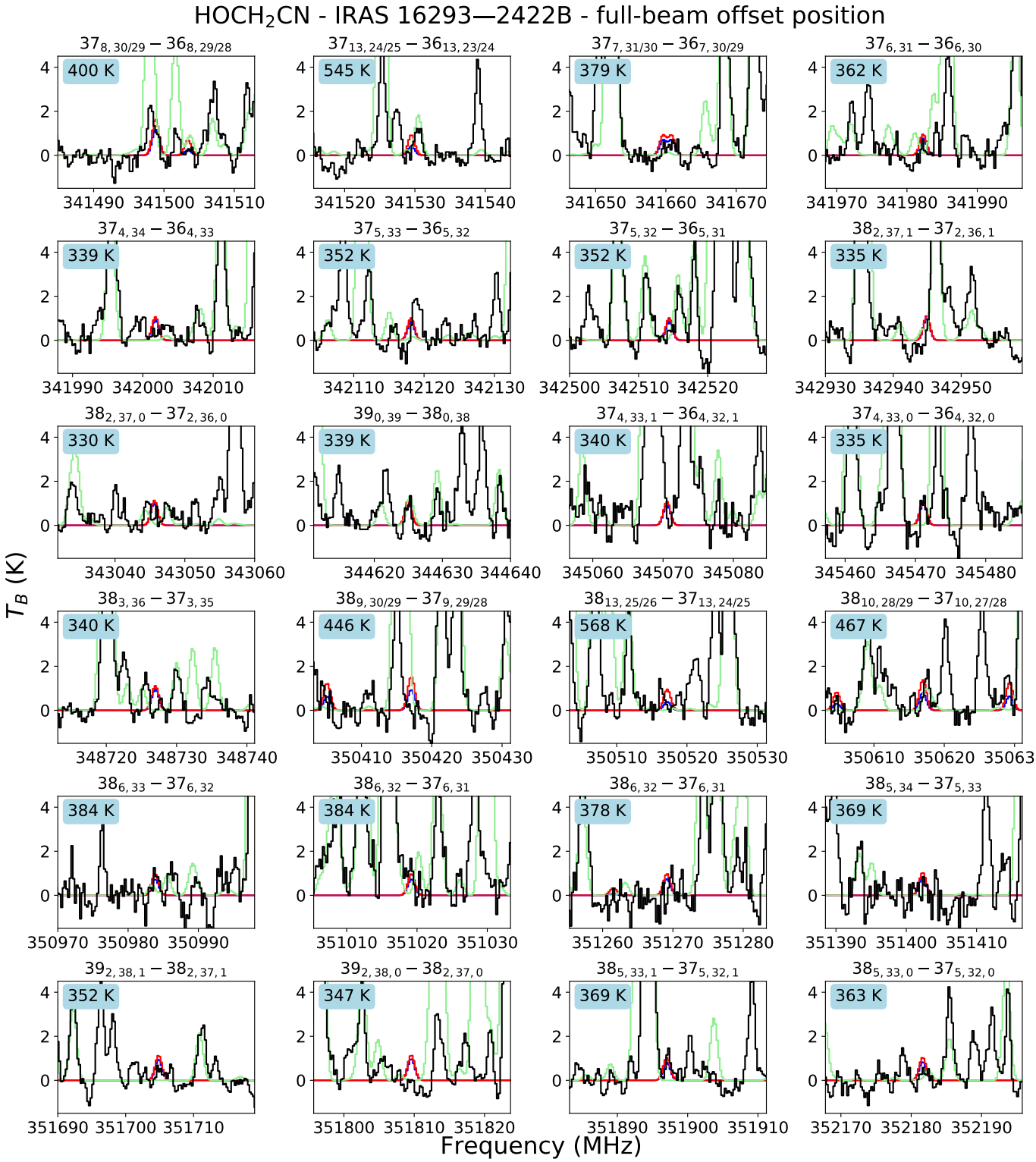


Fig. (C.2) Same as Fig. C.1

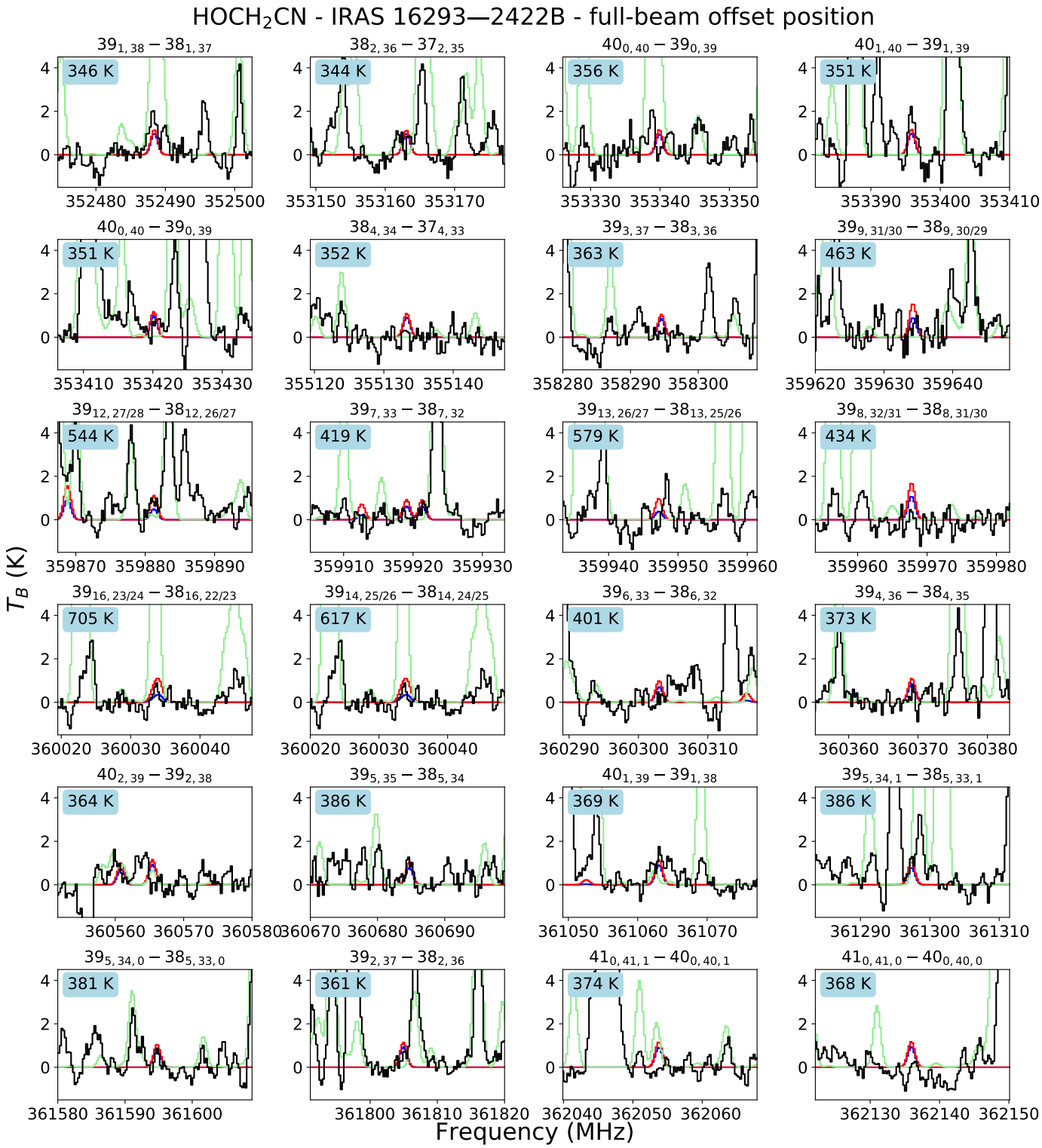


Fig. (C.3) Same as Fig. C.1

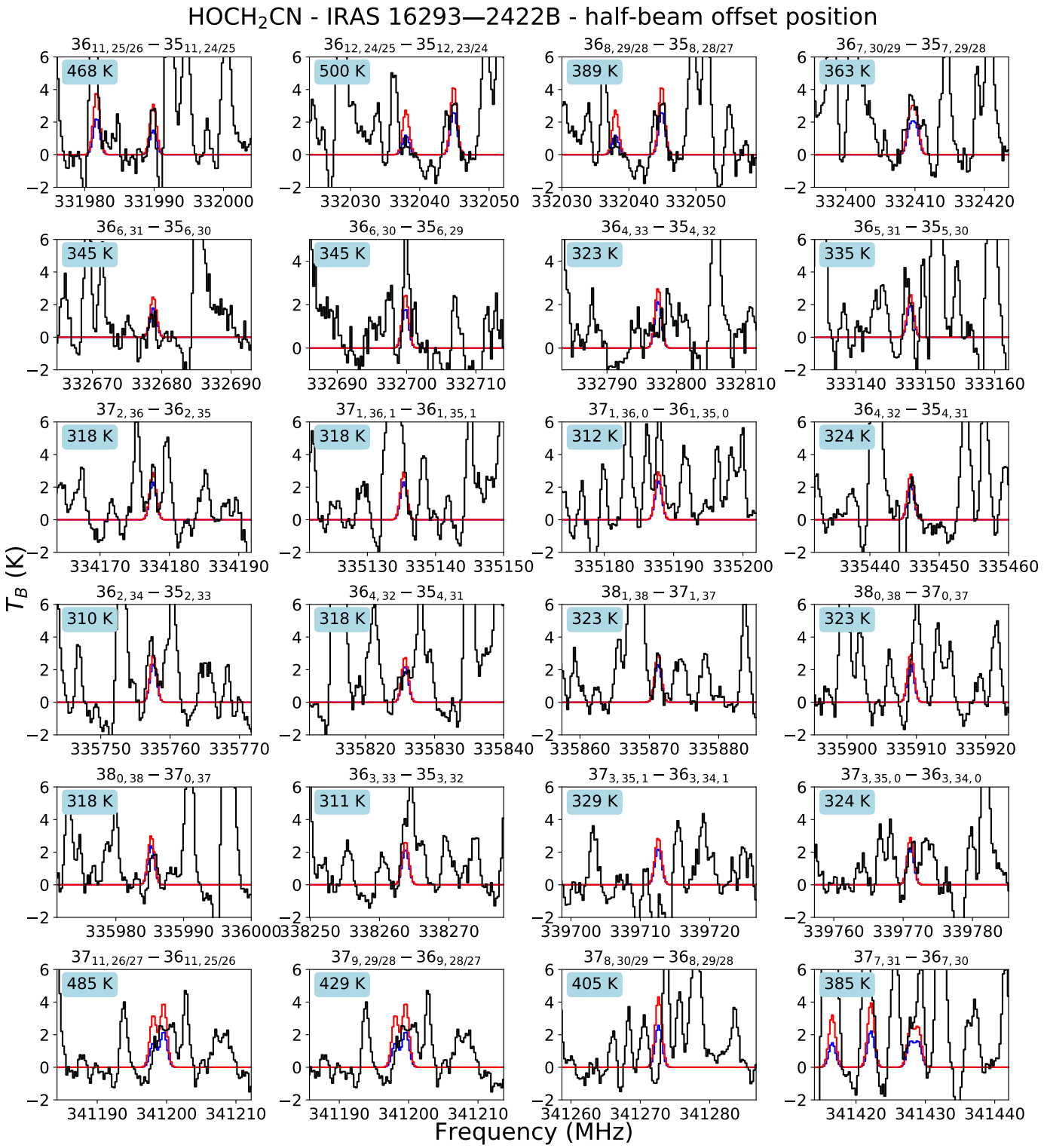


Fig. (C.4) Spectral lines of $HOCH_2CN$ in the PILS spectrum towards IRAS 16293B at the half-beam offset position. The observed spectrum is plotted in black, with synthetic spectra overplotted (N_T = [3.0×10^{15}] cm^{-2}, T_{ex} = 150, blue, and 300 K, red). All covered transitions with $A_{ij} \geq 1.0\times10^{-3}$ s^{-1} that are not blended are shown. The transition is indicated at the top of each panel and the upper state energy is given in the top left of each panel. $HOCH_2CN$ is detected in the half-beam offset position spectrum towards IRAS 16293B.

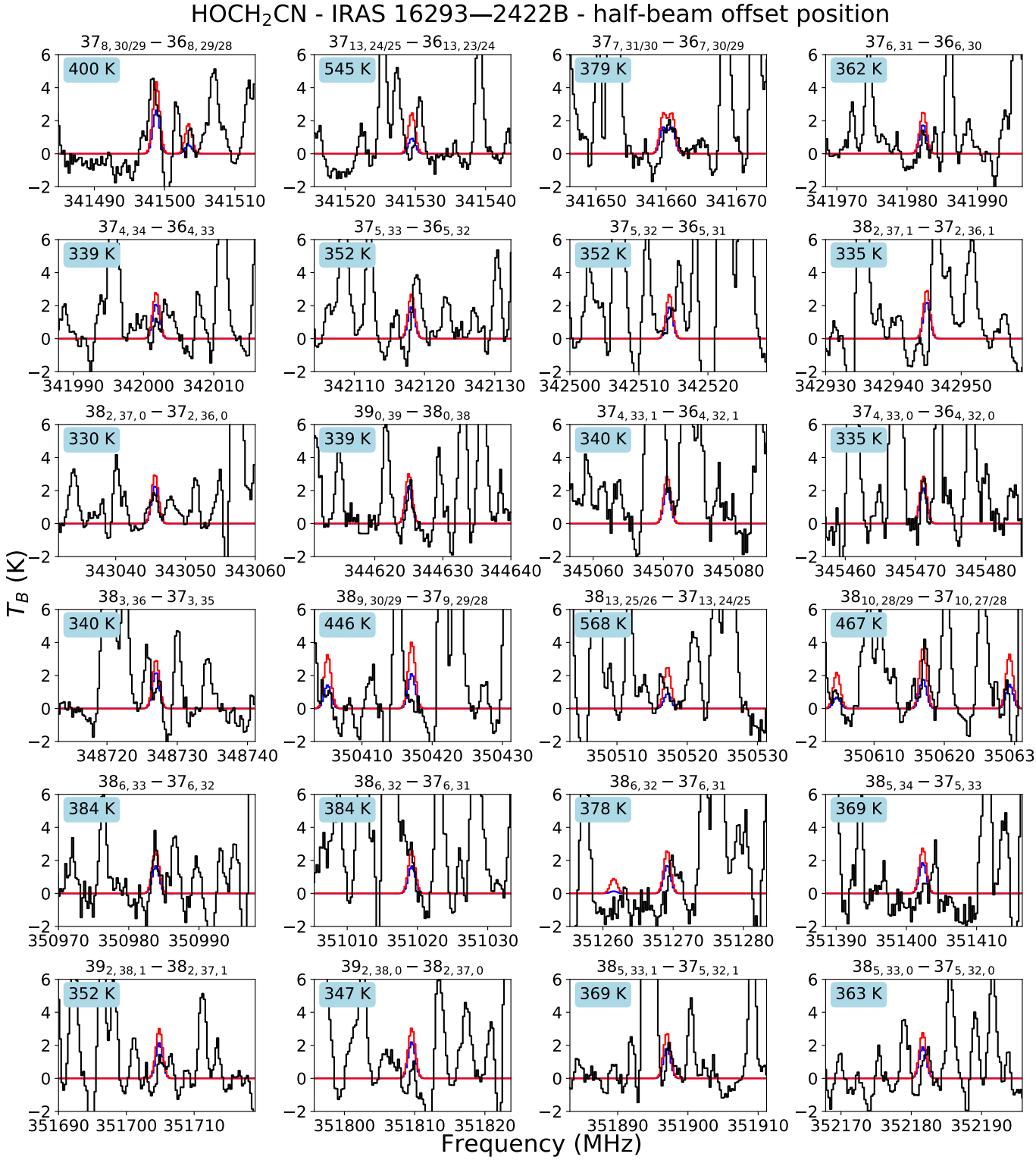


Fig. (C.5) Same as Fig. C.4

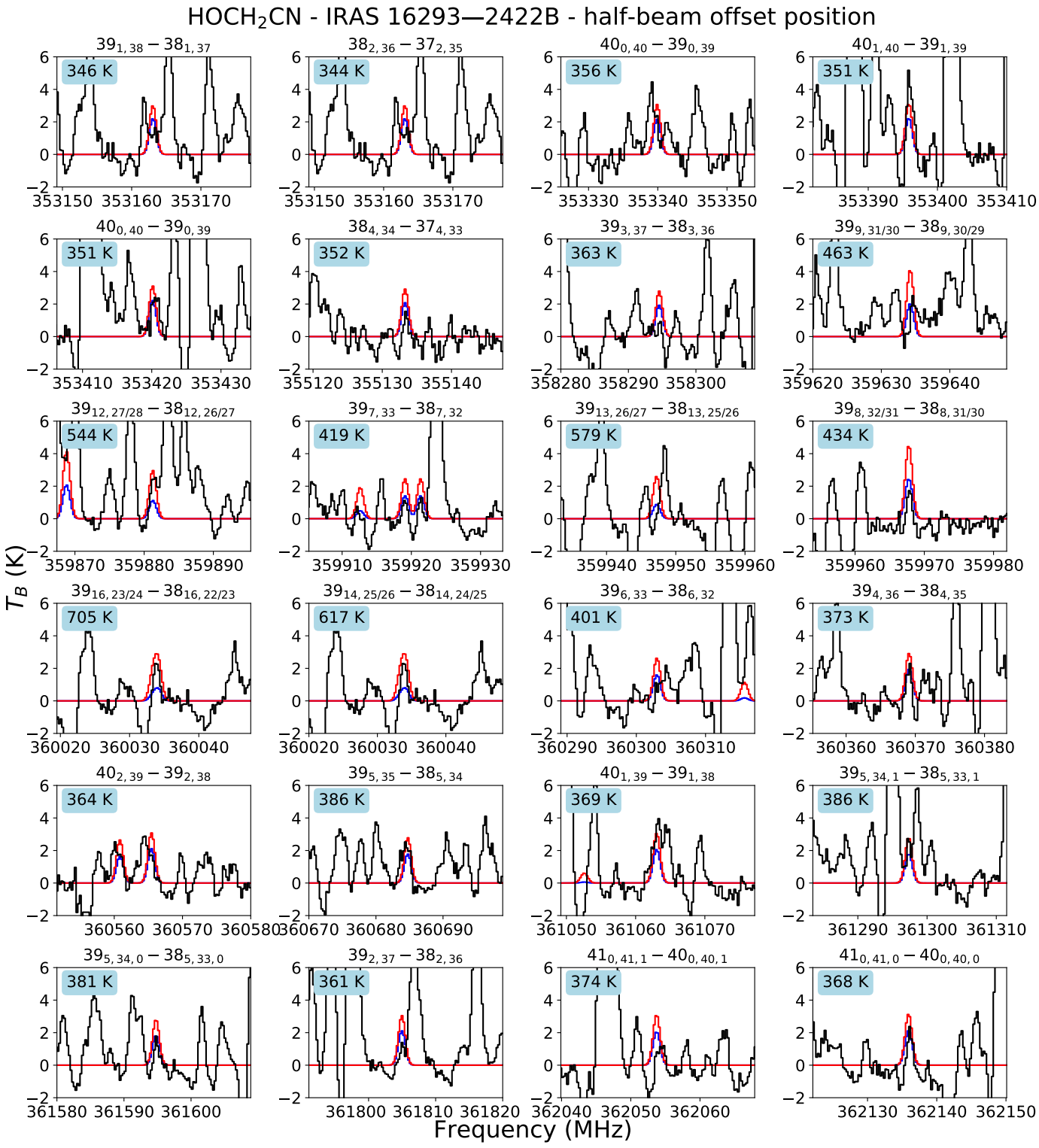


Fig. (C.6) Same as Fig. C.4

Table (B.1) Spectral information of molecules detected towards SMM1-a

Molecule	Database entry	Transition $J, K_a, K_c, (F)$	Frequency (MHz)	E_{up} (K)	A_{ij} s^{-1}
D_2CO	32502	4 2 3 - 3 2 2	233 650.441 (0.0500)	49.63	2.69×10^{-4}
	CDMS	4 3 2 - 3 3 1	234 293.361 (0.0500)	76.62	1.58×10^{-4}
		4 3 1 - 3 3 0	234 331.062 (0.0500)	76.63	1.58×10^{-4}
$^{12}CH_3OH$	32504	15 6 9 3 - 16 5 11 3	217 642.677 (0.0220)	746	1.89×10^{-5}
	CDMS	15 6 10 3 - 16 5 12 3	217 642.678 (0.0220)	746	1.89×10^{-5}
		4 2 3 1 - 3 1 2 1	218 440.063 (0.0130)	45	5.69×10^{-5}
		32 2 30 2 - 32 1 31 1	234 523.365 (0.1070)	1256	8.95×10^{-5}
		4 2 3 0 - 5 1 4 0	234 683.370 (0.0120)	61	1.87×10^{-5}
		5 4 2 2 - 6 3 3 2	234 698.519 (0.0150)	123	6.34×10^{-6}
$CH_3^{18}OH$	34504	5 0 5 0 - 4 0 4 0	231 758.446 (0.0300)	33	5.33×10^{-5}
	CDMS	5 3 3 0 - 4 3 2 0	231 796.218 (0.0300)	83	3.41×10^{-5}
		5 3 2 0 - 4 3 1 0	231 796.521 (0.0300)	83	3.41×10^{-5}
		5 3 2 2 - 4 3 1 2	231 801.304 (0.0300)	81	3.42×10^{-5}
		5 2 4 0 - 4 2 3 0	231 801.466 (0.0300)	71	4.53×10^{-5}
		5 1 4 2 - 4 1 3 2	231 826.744 (0.0300)	54	5.33×10^{-5}
		5 2 3 2 - 4 2 2 2	231 864.501 (0.0300)	56	4.41×10^{-5}
CH_3CN, v_8=1	41509	12 2 2 - 11 -2 2	221 367.450 (0.0011)	649	8.98×10^{-4}
	CDMS	12 -2 2 - 11 2 2	221 367.450 (0.0011)	649	8.98×10^{-4}
		12 4 3 - 11 -4 3	221 380.608 (0.0011)	655	8.21×10^{-4}
		12 -4 3 - 11 4 3	221 380.608 (0.0011)	655	8.21×10^{-4}
		12 1 2 - 11 1 2	221 387.271 (0.0011)	615	9.17×10^{-4}
		12 0 2 - 11 0 2	221 394.085 (0.0011)	594	9.24×10^{-4}
		12 3 3 - 11 3 3	221 403.521 (0.0011)	619	8.66×10^{-4}
		12 1 3 - 11 -1 3	221 625.840 (0.0011)	588	9.20×10^{-4}
NH_2CN	42003	11 1 11 0 - 10 1 10 0	218 461.795 (0.0200)	77	1.08×10^{-3}
	JPL	11 0 11 1 - 10 0 10 1	219 719.651 (0.0200)	135	1.08×10^{-3}
		11 1 10 0 - 10 1 9 0	221 361.160 (0.0200)	78	1.12×10^{-3}
$HN^{12}CO$	43511	10 1 10 - 9 1 9	218 985.696 (0.0192)	101	1.48×10^{-4}
	CDMS	10 2 9 - 9 2 8	219 733.850 (0.0300)	228	1.35×10^{-4}
		10 2 8 - 9 2 7	219 737.193 (0.0300)	228	1.35×10^{-4}
		10 0 10 - 9 0 9	219 798.274 (0.0040)	58	1.47×10^{-4}
		28 1 28 - 29 0 29	231 873.255 (0.0064)	470	6.68×10^{-5}
$HN^{13}CO$	44008	10 1 10 9 - 9 1 9 9	218 984.716 (0.1053)	101	1.63×10^{-6}
		10 1 10 11 - 9 1 9 10	218 985.697 (0.0192)	101	1.48×10^{-4}
		10 1 10 10 - 9 1 9 9	218 985.705 (0.0191)	101	1.46×10^{-4}
		10 1 10 9 - 9 1 9 8	218 985.706 (0.0191)	101	1.46×10^{-4}
		10 1 10 10 - 9 1 9 10	218 986.596 (0.0191)	101	1.48×10^{-6}
		10 1 10 10 - 9 1 9 10	218 986.596 (0.0191)	101	1.48×10^{-6}
		10 2 9 9 - 9 2 8 9	219 739.762 (0.0962)	231	1.60×10^{-6}
		10 2 9 11 - 9 2 8 10	219 740.451 (0.0274)	231	1.45×10^{-4}
		10 2 9 9 - 9 2 8 8	219 740.456 (0.0274)	231	1.43×10^{-4}
		10 2 9 10 - 9 2 8 9	219 740.471 (0.0274)	231	1.43×10^{-4}
		10 2 9 10 - 9 2 8 10	219 741.095 (0.0885)	231	1.45×10^{-6}
		10 2 8 9 - 9 2 7 9	219 743.054 (0.0966)	231	1.60×10^{-6}
		10 2 8 11 - 9 2 7 10	219 743.742 (0.0288)	231	1.45×10^{-4}
		10 2 8 9 - 9 2 7 8	219 743.747 (0.0288)	231	1.43×10^{-4}
		10 2 8 10 - 9 2 7 9	219 743.762 (0.0288)	231	1.43×10^{-4}
		10 2 8 10 - 9 2 7 10	219 744.386 (0.0890)	231	1.45×10^{-6}
		10 0 10 9 - 9 0 9 9	219 803.645 (0.1070)	58	1.67×10^{-6}
		10 0 10 11 - 9 0 9 10	21 9804.439 (0.0171)	58	1.51×10^{-4}
		10 0 10 10 - 9 0 9 9	219 804.442 (0.0171)	58	1.50×10^{-4}
		10 0 10 9 - 9 0 9 8	219 804.446 (0.0171)	58	1.49×10^{-4}
		10 0 10 10 - 9 0 9 10	219 805.163 (0.0965)	58	1.51×10^{-6}
CH_3CH_2OH	46524	35 4 31 2 - 35 3 32 2	218 943.289 (0.0068)	560	7.38×10^{-5}
	CDMS	34 6 28 2 - 34 5 29 2	221 612.904 (0.0080)	548	8.84×10^{-5}
		31 5 27 1 - 31 4 27 0	231 789.850 (0.0120)	506	2.24×10^{-5}

Table (B.1) Continued.

Molecule	Database entry	Transition $J, K_a, K_c, (F)$	Frequency (MHz)	E_{up} (K)	A_{ij} s^{-1}
		22 5 18 2 - 22 4 19 2	231 790.056 (0.0035)	245	8.46×10^{-5}
		13 5 8 2 - 13 4 9 2	233 571.051 (0.0032)	108	7.54×10^{-5}
		14 5 10 2 - 14 4 11 2	233 601.554 (0.0032)	120	7.71×10^{-5}
		12 5 8 2 - 12 4 9 2	234 255.240 (0.0032)	97	7.39×10^{-5}
		11 5 6 2 - 11 4 7 2	234 406.433 (0.0033)	87	7.17×10^{-5}
		10 5 5 2 - 10 4 6 2	234 666.142 (0.0035)	78	6.89×10^{-5}
		10 5 6 2 - 10 4 7 2	234 714.782 (0.0035)	78	6.90×10^{-5}
		23 1 22 2 - 23 0 23 2	234 725.620 (0.0090)	233	3.17×10^{-5}
		9 5 4 2 - 9 4 5 2	234 852.862 (0.0038)	69	6.53×10^{-5}
		36 4 32 2 - 36 3 33 2	234 855.010 (0.0073)	591	8.70×10^{-5}
		9 5 5 2 - 9 4 6 2	234 873.873 (0.0038)	69	6.54×10^{-5}
		14 2 12 1 - 13 3 10 0	234 882.537 (0.0105)	155	3.64×10^{-5}
		14 0 14 1 - 13 1 12 0	235 158.494 (0.0058)	146	1.12×10^{-4}
CH_3NCO, v=0	57505	25 -1 0 2 - 24 -1 0 2	217 595.174 (0.0500)	194	4.84×10^{-4}
	CDMS	25 0 0 2 - 24 0 0 2	217 595.174 (0.0500)	188	4.85×10^{-4}
		25 2 0 1 - 24 2 0 1	217 652.088 (0.0500)	171	4.82×10^{-4}
		24 3 0 1 - 23 3 0 1	217 701.086 (0.0500)	191	4.40×10^{-4}
		25 1 0 -3 - 24 1 0 -3	218 002.461 (0.0500)	258	4.93×10^{-4}
		25 0 0 -3 - 24 0 0 -3	218 014.630 (0.0500)	251	4.84×10^{-4}
		25 1 0 3 - 24 1 0 3	218 069.900 (0.0500)	257	4.93×10^{-4}
		25 1 24 0 - 24 1 23 0	218 541.803 (0.0500)	142	4.94×10^{-4}
		27 -1 0 1 - 26 -1 0 1	231 793.783 (0.0500)	175	6.02×10^{-4}
		27 2 26 0 - 26 2 25 0	234 088.125 (0.0500)	181	6.05×10^{-4}
		27 0 0 2 - 26 0 0 2	234 932.492 (0.0500)	210	6.11×10^{-4}
		27 -3 0 2 - 26 -3 0 2	235 663.096 (0.0500)	264	6.06×10^{-4}
		27 2 0 3 - 26 2 0 3	235 801.163 (0.0500)	296	6.12×10^{-4}
		27 2 0 -3 - 26 2 0 -3	235 803.211 (0.0500)	297	6.12×10^{-4}
$HOCH_2CN$	57512	24 2 23 1 - 23 2 22 1	218 994.156 (0.0009)	143	3.23×10^{-4}
	CDMS	24 8 17 1 - 23 8 16 1	221 334.546 (0.0009)	227	2.98×10^{-4}
		24 8 16 1 - 23 8 15 1	221 334.546 (0.0009)	227	2.98×10^{-4}
		24 9 15 1 - 23 9 14 1	221 344.331 (0.0010)	251	2.88×10^{-4}
		24 9 16 1 - 23 9 15 1	221 344.331 (0.0010)	251	2.88×10^{-4}
		24 10 14 1 - 23 10 13 1	221 372.125 (0.0010)	277	2.77×10^{-4}
		24 10 15 1 - 23 10 14 1	221 372.125 (0.0010)	277	2.77×10^{-4}
		24 6 19 1 - 23 6 18 1	221 406.933 (0.0009)	188	3.15×10^{-4}
		24 6 18 1 - 23 6 17 1	221 407.170 (0.0009)	188	3.15×10^{-4}
		24 11 13 1 - 23 11 12 1	221 413.638 (0.0010)	306	2.65×10^{-4}
		24 11 14 1 - 23 11 13 1	221 413.638 (0.0010)	306	2.65×10^{-4}
		24 12 12 1 - 23 12 11 1	221 466.304 (0.0011)	338	2.52×10^{-4}
		24 12 13 1 - 23 12 12 1	221 466.304 (0.0011)	338	2.52×10^{-4}
		24 3 22 1 - 23 3 21 1	221 466.604 (0.0009)	151	3.32×10^{-4}
		24 8 17 0 - 23 8 16 0	221 480.199 (0.0009)	222	2.95×10^{-4}
		24 8 16 0 - 23 8 15 0	221 480.199 (0.0009)	222	2.95×10^{-4}
		24 9 15 0 - 23 9 14 0	221 488.785 (0.0010)	245	2.86×10^{-4}
		24 9 16 0 - 23 9 15 0	221 488.785 (0.0010)	245	2.86×10^{-4}
		24 7 18 0 - 23 7 17 0	221 497.997 (0.0009)	201	3.04×10^{-4}
		24 7 17 0 - 23 7 16 0	221 498.002 (0.0009)	201	3.04×10^{-4}
		24 10 14 0 - 23 10 13 0	221 515.800 (0.0010)	272	2.75×10^{-4}
		24 10 15 0 - 23 10 14 0	221 515.800 (0.0010)	272	2.75×10^{-4}
		24 13 11 1 - 23 13 10 1	221 528.501 (0.0011)	372	2.38×10^{-4}
		24 13 12 1 - 23 13 11 1	221 528.501 (0.0011)	372	2.38×10^{-4}
		24 5 20 1 - 23 5 19 1	221 533.058 (0.0009)	173	3.22×10^{-4}
		24 5 19 1 - 23 5 18 1	221 542.097 (0.0009)	173	3.22×10^{-4}
		24 11 13 0 - 23 11 12 0	221 556.802 (0.0010)	301	2.63×10^{-4}
		24 11 14 0 - 23 11 13 0	221 556.802 (0.0010)	301	2.63×10^{-4}
		24 6 19 0 - 23 6 18 0	221 557.660 (0.0009)	183	3.12×10^{-4}
		24 6 18 0 - 23 6 17 0	221 557.911 (0.0009)	183	3.12×10^{-4}

Table (B.1) Continued.

Molecule	Database entry	Transition $J, K_a, K_c, (F)$	Frequency (MHz)	E_{up} (K)	A_{ij} s^{-1}
		24 12 12 0 - 23 12 11 0	221 609.140 (0.0010)	332	2.50×10^{-4}
		24 12 13 0 - 23 12 12 0	221 609.140 (0.0010)	332	2.50×10^{-4}
		25 2 23 1 - 24 2 22 1	234 584.932 (0.0300)	157	4.36×10^{-4}
		25 2 23 0 - 24 2 22 0	235 112.110 (0.0300)	152	3.94×10^{-4}
CH_3OCHO	60003	18 10 9 3 - 17 10 8 3	219 822.126 (0.1000)	355	1.11×10^{-4}
	JPL	18 10 8 3 - 17 10 7 3	219 822.126 (0.1000)	355	1.11×10^{-4}
		18 11 7 0 - 17 11 6 0	221 433.019 (0.1000)	181	1.03×10^{-4}
		18 11 8 0 - 17 11 7 0	221 433.019 (0.1000)	181	1.03×10^{-4}
		18 10 8 2 - 17 10 7 2	221 649.411 (0.1000)	167	1.14×10^{-4}
		19 4 16 4 - 18 4 15 4	231 896.060 (0.1000)	310	1.79×10^{-4}
		19 8 12 4 - 18 8 11 4	233 627.478 (0.1000)	341	1.59×10^{-4}
		19 10 10 0 - 18 10 9 0	234 124.883 (0.1000)	179	1.40×10^{-4}
		19 10 9 0 - 18 10 8 0	234 124.883 (0.1000)	179	1.40×10^{-4}
		19 10 10 1 - 18 10 9 1	234 134.600 (0.0500)	178	1.40×10^{-4}
		19 6 14 3 - 18 6 13 3	234 336.107 (0.1000)	324	1.75×10^{-4}
		19 5 15 3 - 18 5 14 3	234 381.269 (0.1000)	316	1.80×10^{-4}
		19 7 13 4 - 18 7 12 4	234 441.264 (0.1000)	332	1.68×10^{-4}
		19 9 10 2 - 18 9 9 2	234 486.395 (0.1000)	166	1.51×10^{-4}
		19 9 11 0 - 18 9 10 0	234 502.241 (0.0009)	166	1.51×10^{-4}
		19 9 10 0 - 18 9 9 0	234 502.432 (0.0009)	166	1.51×10^{-4}
		19 9 11 1 - 18 9 10 1	234 508.614 (0.1000)	166	1.51×10^{-4}
		19 8 11 2 - 18 8 10 2	235 029.952 (0.1000)	155	1.61×10^{-4}
		19 8 12 0 - 18 8 11 0	235 046.493 (0.1000)	155	1.61×10^{-4}
		19 8 11 0 - 18 8 10 0	235 051.378 (0.1000)	155	1.61×10^{-4}
		19 8 12 1 - 18 8 11 1	235 051.378 (0.1000)	155	1.61×10^{-4}
		19 6 13 5 - 18 6 12 5	235 084.738 (0.1000)	324	1.76×10^{-4}
		20 3 18 4 - 19 3 17 4	235 200.422 (0.1000)	314	1.90×10^{-4}
		19 5 15 4 - 18 5 14 4	235 633.058 (0.1000)	316	1.81×10^{-4}
		19 7 13 0 - 18 7 12 0	235 844.544 (0.1000)	145	1.71×10^{-4}
		19 7 13 1 - 18 7 12 1	235 865.969 (0.1000)	145	1.67×10^{-4}
		20 2 18 3 - 19 2 17 3	235 904.655 (0.1000)	315	1.91×10^{-4}
		21 2 20 3 - 20 2 19 3	235 919.352 (0.1000)	319	1.94×10^{-4}
		19 7 12 0 - 18 7 11 0	235 932.379 (0.1000)	145	1.72×10^{-4}
a-$(CH_2OH)_2$	62503	22 14 8 0 - 21 14 7 1	218 468.381 (0.0044)	221	1.51×10^{-4}
	CDMS	22 14 9 0 - 21 14 8 1	218 468.381 (0.0044)	221	1.51×10^{-4}
		20 4 16 1 - 19 4 15 0	219 764.925 (0.0040)	114	2.45×10^{-4}
		22 8 14 0 - 21 8 13 1	219 809.406 (0.0026)	156	2.24×10^{-4}
		28 12 16 0 - 28 11 17 0	233 426.949 (0.0036)	270	3.11×10^{-5}
		28 12 17 0 - 28 11 18 0	233 427.018 (0.0036)	270	3.10×10^{-5}
		28 12 16 1 - 28 11 17 1	233 451.651 (0.0036)	271	3.32×10^{-5}
		28 12 17 1 - 28 11 18 1	233 451.723 (0.0036)	271	3.32×10^{-5}
		22 5 18 1 - 21 5 17 0	233 536.696 (0.0025)	138	2.93×10^{-4}
		22 7 16 1 - 21 7 15 0	233 561.784 (0.0024)	149	2.79×10^{-4}
		22 6 17 1 - 21 6 16 0	234 264.446 (0.0026)	143	2.84×10^{-4}
		51 13 39 1 - 51 12 40 1	235 170.476 (0.0288)	737	4.73×10^{-5}
		23 3 21 1 - 22 3 20 0	235 170.573 (0.0023)	139	2.91×10^{-4}
		22 6 16 1 - 21 6 15 0	235 304.050 (0.0026)	143	2.90×10^{-4}
		14 5 9 1 - 13 4 10 1	235 326.413 (0.0021)	64	2.39×10^{-5}
		21 4 18 0 - 20 3 17 0	235 327.161 (0.0027)	122	6.30×10^{-5}
		23 2 21 1 - 22 2 20 0	235 600.178 (0.0022)	139	3.28×10^{-4}
		24 4 21 0 - 23 4 20 1	235 620.372 (0.0027)	155	2.88×10^{-4}
		26 1 26 0 - 25 1 25 1	235 834.239 (0.0040)	159	3.22×10^{-4}
		26 0 26 0 - 25 0 25 1	235 834.327 (0.0040)	159	3.22×10^{-4}

Table (C.1) Molecules and parameters used for the IRAS 16293B synthetic spectrum

Molecule	Name	Tag	Database	N_T (cm^{-2})	T_{ex} (K)
CCH	Ethynyl radical	25501	CDMS	3.00×10^{13}	120
HCN	Hydrogen cyanide	27501	CDMS	5.00×10^{16}	120
HNC	Hydrogen isocyanide	27502	CDMS	5.00×10^{16}	120
$H^{13}CN$	Hydrogen cyanide	28501	CDMS	2.00×10^{14}	300
CO	Carbon monoxide	28503	CDMS	1.00×10^{20}	100
$HC^{15}N$	Hydrogen cyanide	28506	CDMS	2.00×10^{14}	300
DNC	Hydrogen cyanide	28508	CDMS	7.00×10^{14}	300
^{13}CO	Carbon monoxide	29501	CDMS	3.10×10^{19}	100
$C^{17}O$	Carbon monoxide	29503	CDMS	8.00×10^{16}	100
$H^{13}C^{15}$	Hydrogen cyanide	29512	CDMS	2.00×10^{14}	300
$HNCH_2$	Methanimine	29518	CDMS	8.00×10^{14}	100
NO	Nitrogen oxide	30008	JPL	2.00×10^{16}	100
H_2CO	Formaldehyde	30501	CDMS	1.80×10^{18}	105
$C^{18}O$	Carbon monoxide	30502	CDMS	1.00×10^{17}	100
DCO^+	Formyl radical	30510	CDMS	3.00×10^{12}	29
CH_3NH_2	Methylamine	31008	JPL	5.30×10^{14}	100
HDCO	Formaldehyde	31501	CDMS	1.30×10^{17}	105
$H_2^{13}CO$	Formaldehyde	31503	CDMS	3.60×10^{16}	105
D_2CO	Formaldehyde	32502	CDMS	1.60×10^{16}	105
$H_2C^{18}O$	Formaldehyde	32503	CDMS	2.50×10^{15}	105
CH_3OH	Methanol	32504	CDMS	2.00×10^{19}	300
CH_2DOH	Methanol	33004	JPL	7.10×10^{17}	300
$^{13}CH_3OH$	Methanol	33502	CDMS	4.00×10^{16}	300
NH_2OH	Hydroxylamine	33503	CDMS	3.70×10^{14}	100
$D_2^{13}CO$	Formaldehyde	33506	CDMS	2.20×10^{14}	105
$HDC^{18}O$	Formaldehyde	33510	CDMS	1.40×10^{14}	105
H_2S	Hydrogen sulfide	34502	CDMS	1.00×10^{18}	125
$CH_3^{18}OH$	Methanol	34504	CDMS	2.00×10^{16}	300
HDS	Hydrogen sulfide	35502	CDMS	2.00×10^{16}	125
$HD^{34}S$	Hydrogen sulfide	37503	CDMS	1.00×10^{15}	125
c-C_3H_2	Cyclopropenylidene	38508	CDMS	2.00×10^{14}	100
CH_3CCH	Propyne	40502	CDMS	6.80×10^{15}	100
CH_3CN	Acetonitrile	41505	CDMS	4.00×10^{16}	120
CH_3CN ν_8=1	Acetonitrile	41509	CDMS	4.00×10^{16}	120
CH_3NC	Methyl isocyanide	41514	CDMS	2.00×10^{14}	150
H_2CCO	Ketene	42501	CDMS	4.80×10^{16}	125
HNCNH	Carbodiimide	42506	CDMS	2.40×10^{16}	300
$^{13}CH_3CN$	Acetonitrile	42508	CDMS	3.30×10^{14}	130
$CH_3^{13}CN$	Acetonitrile	42509	CDMS	3.00×10^{14}	130
$CH_3C^{15}N$	Acetonitrile	42510	CDMS	8.70×10^{13}	130
CH_2DCN	Acetonitrile	42511	CDMS	5.60×10^{14}	130
$H_2C^{13}CO$	Ketene	43505	CDMS	7.10×10^{14}	125
$H_2^{13}CCO$	Ketene	43506	CDMS	7.10×10^{14}	125
HDC_2O	Ketene	43507	CDMS	2.00×10^{15}	125
HNCO	Isocyanic acid	43511	CDMS	3.70×10^{16}	300
CHD_2CN	Acetonitrile	43514	CDMS	1.20×10^{14}	130
$H_2N^{13}CN$	Cyanamide	43515	CDMS	3.00×10^{13}	300
N_2O	Nitrous oxide	44004	JPL	5.00×10^{16}	100
DNCO	Isocyanic acid	44006	JPL	3.00×10^{14}	300
$HN^{13}CO$	Isocyanic acid	44008	JPL	4.00×10^{14}	300
CS	Carbon monosulfide	44501	CDMS	1.00×10^{16}	125
c-C_2H_4O	Ethylene oxide	44504	CDMS	4.10×10^{15}	125
SiO	Silicon monoxide	44505	CDMS	7.00×10^{13}	300
s-H_2CCHOH	Vinylalcohol	44506	CDMS	1.20×10^{17}	125
a-H_2CCHOH	Vinylalcohol	44507	CDMS	1.20×10^{17}	125
$C^{33}S$	Carbon monosulfide	45502	CDMS	1.00×10^{14}	125

Table (C.1) Continued.

Molecule	Name	Tag	Database	N_T (cm^{-2})	T_{ex} (K)
NH_2CHO	Formamide	45512	CDMS	1.00×10^{16}	300
CH_3CDO	Acetaldehyde	45524	CDMS	7.40×10^{15}	125
CH_2DCHO	Acetaldehyde	45525	CDMS	6.20×10^{15}	125
$C^{34}S$	Carbon monosulfide	46501	CDMS	3.00×10^{14}	125
t-HCOOH	Formic acid	46506	CDMS	5.08×10^{16}	300
H_2CS	Thioformaldehyde	46509	CDMS	1.50×10^{15}	125
$NH_2^{13}CHO$	Formamide	46512	CDMS	1.00×10^{14}	300
CH_3OCH_3	Dimethyl ether	46514	CDMS	3.00×10^{17}	125
NH_2CDO	Formamide	46520	CDMS	1.40×10^{14}	300
cis-NHDCHO	Formamide	46521	CDMS	1.40×10^{14}	300
trans-NHDCHO	Formamide	46522	CDMS	1.20×10^{14}	300
C_2H_5OH	Ethanol	46524	CDMS	2.30×10^{17}	300
HONO	Nitrous acid	47007	JPL	9.00×10^{14}	100
t-$H^{13}COOH$	Formic acid	47503	CDMS	8.30×10^{14}	300
HDCS	Thioformaldehyde	47504	CDMS	1.50×10^{14}	125
$CH_3^{13}CH_2OH$	Ethanol	47511	CDMS	4.60×10^{14}	300
$^{13}CH_3CH_2OH$	Ethanol	47512	CDMS	4.60×10^{14}	300
CH_3CH_2OD	Ethanol	47515	CDMS	5.75×10^{14}	300
CH_3CHDOH	Ethanol	47516	CDMS	1.15×10^{15}	300
a-CH_2DCH_2OH	Ethanol	47517	CDMS	1.34×10^{15}	300
s-CH_2DCH_2OH	Ethanol	47518	CDMS	6.51×10^{14}	300
SO	Sulfur monoxide	48501	CDMS	5.00×10^{14}	125
$C^{36}S$	Carbon monosulfide	48503	CDMS	2.00×10^{13}	125
CH_3SH	Methyl mercaptan	48510	CDMS	5.50×10^{15}	125
$CH_3^{35}Cl$	Chloromethane	50007	JPL	3.10×10^{13}	125
HC_3N	Cyanoacetylene	51501	CDMS	1.40×10^{14}	100
$CH_3^{37}Cl$	Chloromethane	52009	JPL	2.20×10^{14}	125
C_2H_3CN	Vinyl cyanide	53515	CDMS	4.80×10^{14}	110
C_2H_5CN	Ethyl cyanide	55502	CDMS	1.50×10^{15}	160
CH_3NCO	Methyl isocyanate	57505	CDMS	3.00×10^{15}	300
$CH_3C(O)CH_3$	Acetone	58003	JPL	3.40×10^{16}	125
CH_3CH_2CHO	Propanal	58505	CDMS	1.48×10^{15}	125
CH_3OCHO	Methylformate	60003	JPL	2.60×10^{17}	300
$HOCH_2CHO$	Glycolaldehyde	60501	CDMS	3.40×10^{16}	300
OCS	Carbonyl sulfide	60503	CDMS	2.00×10^{16}	125
OCS v_2=1	Carbonyl sulfide	60504	CDMS	2.00×10^{17}	125
CH_3COOH	Acetic acid	60523	CDMS	3.00×10^{15}	300
$O^{13}CS$	Carbonyl sulfide	61502	CDMS	5.00×10^{15}	125
$OC^{33}S$	Carbonyl sulfide	61503	CDMS	3.00×10^{15}	100
$HOCH_2^{13}CHO$	Glycolaldehyde	61513	CDMS	4.46×10^{14}	300
$HO^{13}CH_2CHO$	Glycolaldehyde	61514	CDMS	4.46×10^{14}	300
$CH_3O^{13}CHO$	Glycolaldehyde	61515	CDMS	6.30×10^{15}	300
$DOCH_2CHO$	Glycolaldehyde	61516	CDMS	4.86×10^{14}	300
HOCHDCHO	Glycolaldehyde	61517	CDMS	1.27×10^{15}	300
$HOCH_2CDO$	Glycolaldehyde	61518	CDMS	6.25×10^{14}	300
a-$(CH_2OH)_2$	Ethylene glycol	62503	CDMS	1.37×10^{16}	300
s-$(CH_2OH)_2$	Ethylene glycol	62504	CDMS	3.62×10^{16}	300
$OC^{34}S$	Carbonyl sulfide	62505	CDMS	1.50×10^{16}	125
^{18}OCS	Carbonyl sulfide	62506	CDMS	7.00×10^{14}	125
SO_2	Sulfur dioxide	64502	CDMS	1.50×10^{15}	125
$^{34}O_2$	Sulfur dioxide	66501	CDMS	4.00×10^{14}	125

Table (C.1) $HOCH_2CN$ lines in the PILS data towards IRAS 16293B

Transition J, K_a, K_c, F	Frequency (MHz)	E_{up} (K)	A_{ij} s^{-1}	Blending species
36 11 25 1 - 35 11 24 1	331 990.003	468	1.03×10^{-3}	g-$(CH_2OH)_2$
36 11 26 1 - 35 11 25 1	331 990.003	468	1.03×10^{-3}	g-$(CH_2OH)_2$
36 12 24 1 - 35 12 23 1	332 038.123	500	1.01×10^{-3}	CH_3OCHO
36 12 25 1 - 35 12 24 1	332 038.123	500	1.01×10^{-3}	CH_3OCHO
36 8 29 1 - 35 8 28 1	332 045.021	389	1.08×10^{-3}	g-$(CH_2OH)_2$
36 8 28 1 - 35 8 27 1	332 045.044	389	1.08×10^{-3}	g-$(CH_2OH)_2$
36 7 30 0 - 35 7 29 0	332 409.418	363	1.09×10^{-3}	–
36 7 29 0 - 35 7 28 0	332 410.281	363	1.09×10^{-3}	–
36 6 31 0 - 35 6 30 0	332 678.904	345	1.10×10^{-3}	–
36 6 30 0 - 35 6 29 0	332 699.957	345	1.10×10^{-3}	–
36 4 33 1 - 35 4 32 1	332 797.489	323	1.14×10^{-3}	–
36 5 31 1 - 35 5 30 1	333 147.976	335	1.13×10^{-3}	–
37 2 36 1 - 36 2 35 1	334 177.762	318	1.15×10^{-3}	CH_3OCHO, $CH_3O^{13}CHO$, C_2H_5CN, $HO^{13}CH_2CHO$
37 1 36 1 - 36 1 35 1	335 135.448	318	1.16×10^{-3}	CH_3OH
37 1 36 0 - 36 1 35 0	335 187.943	313	1.16×10^{-3}	–
36 4 32 1 - 35 4 31 1	335 446.009	324	1.17×10^{-3}	–
36 2 34 1 - 35 2 33 1	335 757.704	310	1.15×10^{-3}	g-$(CH_2OH)_2$
36 4 32 0 - 35 4 31 0	335 825.850	318	1.15×10^{-3}	g-$(CH_2OH)_2$, $CH_3C(O)CH_3$, CH_3OCHO
38 1 38 1 - 37 1 37 1	335 871.388	323	1.17×10^{-3}	–
38 0 38 1 - 37 0 37 1	335 909.319	323	1.17×10^{-3}	–
38 0 38 0 - 37 0 37 0	335 985.342	318	1.17×10^{-3}	CH_3CH_2OH, g-$(CH_2OH)_2$
36 3 33 0 - 35 3 32 0	338 263.867	311	1.07×10^{-3}	CH_3OCHO
37 3 35 1 - 36 3 34 1	339 712.712	329	1.21×10^{-3}	NH_2CHO
37 3 35 0 - 36 3 34 0	339 771.178	324	1.20×10^{-3}	–
37 11 26 1 - 36 11 25 1	341 198.194	484	1.13×10^{-3}	–
37 11 27 1 - 36 11 26 1	341 198.194	484	1.13×10^{-3}	–
37 9 29 1 - 36 9 28 1	341 199.695	429	1.16×10^{-3}	g-$(CH_2OH)_2$
37 9 28 1 - 36 9 27 1	341 199.696	429	1.16×10^{-3}	g-$(CH_2OH)_2$
37 8 30 1 - 36 8 29 1	341 272.746	405	1.18×10^{-3}	$HOCH_2CHO$, CH_3CDO
37 8 29 1 - 36 8 28 1	341 272.781	405	1.18×10^{-3}	$HOCH_2CHO$, CH_3CDO
37 7 31 1 - 36 7 30 1	341 427.962	385	1.20×10^{-3}	CH_3CHO
37 8 30 0 - 36 8 29 0	341 498.917	400	1.17×10^{-3}	CH_3OCHO
37 8 29 0 - 36 8 28 0	341 498.954	400	1.17×10^{-3}	CH_3OCHO
37 13 24 0 - 36 13 23 0	341 529.626	545	1.08×10^{-3}	a-$(CH_2OH)_2$
37 13 25 0 - 36 13 24 0	341 529.626	545	1.08×10^{-3}	a-$(CH_2OH)_2$
37 7 31 0 - 36 7 30 0	341 659.715	379	1.18×10^{-3}	–
37 7 30 0 - 36 7 29 0	341 660.941	379	1.18×10^{-3}	–
37 6 31 0 - 36 6 30 0	341 982.421	362	1.20×10^{-3}	$CH_3O^{13}CHO$
37 4 34 1 - 36 4 33 1	342 001.917	339	1.23×10^{-3}	–
37 5 33 1 - 36 5 32 1	342 118.267	352	1.23×10^{-3}	$HOCH_2CHO$
37 5 32 1 - 36 5 31 1	342 514.548	352	1.23×10^{-3}	CH_3CDO
38 2 37 1 - 37 2 36 1	342 945.040	335	1.25×10^{-3}	H_2CS, $CH_3O^{13}CHO$
38 2 37 0 - 37 2 36 0	343 045.762	330	1.24×10^{-3}	CH_3CDO
39 0 39 1 - 38 0 38 1	344 625.126	339	1.27×10^{-3}	HONO, CH_2DOH, CH_3CHO
37 4 33 1 - 36 4 32 1	345 070.674	340	1.27×10^{-3}	CH_3OCHO
37 4 33 0 - 36 4 32 0	345 471.229	335	1.25×10^{-3}	CH_3OCHO
38 3 36 0 - 37 3 35 0	348 727.094	340	1.30×10^{-3}	–
38 9 30 1 - 37 9 29 1	350 417.202	446	1.27×10^{-3}	a-$(CH_2OH)_2$
38 9 29 1 - 37 9 28 1	350 417.203	446	1.27×10^{-3}	a-$(CH_2OH)_2$
38 13 25 1 - 37 13 24 1	350 517.318	568	1.19×10^{-3}	–
38 13 26 1 - 37 13 25 1	350 517.318	568	1.19×10^{-3}	–
38 10 28 0 - 37 10 27 0	350 617.089	467	1.24×10^{-3}	$CH_3O^{13}CHO$
38 10 29 0 - 37 10 28 0	350 617.089	467	1.24×10^{-3}	$CH_3O^{13}CHO$
38 6 33 1 - 37 6 32 1	350 983.970	384	1.32×10^{-3}	CH_3OCHO, CH_3CDO
38 6 32 1 - 37 6 31 1	351 019.318	384	1.32×10^{-3}	$H_2C^{13}CO$, CH_3OCHO
38 6 32 0 - 37 6 31 0	351 269.282	378	1.30×10^{-3}	–
38 5 34 1 - 37 5 33 1	351 402.459	369	1.33×10^{-3}	–

Table (C.1) Continued.

Transition J, K_a, K_c, F	Frequency (MHz)	E_{up} (K)	A_{ij} s^{-1}	Blending species
39 2 38 1 - 38 2 37 1	351 704.972	352	1.35×10^{-3}	–
39 2 38 0 - 38 2 37 0	351 809.704	346	1.34×10^{-3}	–
38 5 33 1 - 37 5 32 1	351 897.151	369	1.34×10^{-3}	–
38 5 33 0 - 37 5 32 0	352 181.763	363	1.32×10^{-3}	$CH_3O^{13}CHO$
39 1 38 0 - 38 1 37 0	352 488.531	346	1.35×10^{-3}	$CH_3^{18}OH$
38 2 36 1 - 37 2 35 1	353 163.191	344	1.35×10^{-3}	–
40 0 40 1 - 39 0 39 1	353 340.026	356	1.37×10^{-3}	CH_3OCHO
40 1 40 0 - 39 1 39 0	353 395.992	351	1.37×10^{-3}	–
40 0 40 0 - 39 0 39 0	353 420.250	351	1.37×10^{-3}	–
38 4 34 0 - 37 4 33 0	355 133.419	352	1.36×10^{-3}	–
39 3 37 1 - 38 3 36 1	358 294.680	363	1.33×10^{-3}	–
39 9 31 1 - 38 9 30 1	359 634.337	463	1.37×10^{-3}	–
39 9 30 1 - 38 9 29 1	359 634.339	463	1.37×10^{-3}	–
39 12 27 0 - 38 12 26 0	359 881.373	545	1.30×10^{-3}	–
39 12 28 0 - 38 12 27 0	359 881.373	545	1.30×10^{-3}	–
39 7 33 1 - 38 7 32 1	359 919.218	419	1.41×10^{-3}	–
39 13 26 0 - 38 13 25 0	359 947.354	579	1.28×10^{-3}	–
39 13 27 0 - 38 13 26 0	359 947.354	579	1.28×10^{-3}	–
39 8 32 0 - 38 8 31 0	359 967.849	434	1.38×10^{-3}	–
39 8 31 0 - 38 8 30 0	359 967.931	434	1.38×10^{-3}	–
39 16 23 1 - 38 16 22 1	360 033.494	705	1.21×10^{-3}	t-HCOOH
39 16 24 1 - 38 16 23 1	360 033.494	705	1.21×10^{-3}	t-HCOOH
39 14 25 0 - 38 14 24 0	360 034.284	617	1.25×10^{-3}	t-HCOOH
39 14 26 0 - 38 14 25 0	360 034.284	617	1.25×10^{-3}	t-HCOOH
39 6 33 1 - 38 6 32 1	360 303.101	401	1.43×10^{-3}	–
39 4 36 1 - 38 4 35 1	360 369.224	373	1.45×10^{-3}	–
40 2 39 0 - 39 2 38 0	360 565.572	364	1.44×10^{-3}	–
39 5 35 1 - 38 5 34 1	360 684.867	386	1.44×10^{-3}	–
40 1 39 1 - 39 1 38 1	361 063.161	369	1.46×10^{-3}	–
39 5 34 1 - 38 5 33 1	361 297.474	386	1.45×10^{-3}	CH_3CH_2OH
39 5 34 0 - 38 5 33 0	361 594.894	381	1.43×10^{-3}	–
39 2 37 1 - 38 2 36 1	361 805.086	361	1.46×10^{-3}	CH_3OCHO
41 0 41 1 - 40 0 40 1	362 053.851	374	1.47×10^{-3}	$CH_3C(O)CH_3$
41 0 41 0 - 40 0 40 0	362 136.053	368	1.47×10^{-3}	–

Notes. List of identified and unidentified $HOCH_2CN$ transitions with $A_{ij} \geq 1.0\times10^{-3}$ s^{-1} towards IRAS 16293B in the PILS data set.